JM PAPERS

Statistical characterization of a shock interacting with an inclined gas column

Brian E. Romero[1,†], **Jon M. Reisner**[1], **Peter Vorobieff**[2] and **Svetlana V. Poroseva**[2]

[1]Computational Physics Division, Los Alamos National Laboratories, Los Alamos, NM 87545, USA

[2]Department of Mechanical Engineering, University of New Mexico, Albuquerque, NM 87131, USA

We present a statistical characterization of the interaction between a planar shock and a finite-diameter, cylindrical column of dense gas based on three-dimensional, large-eddy simulation results. In the simulation, the column of gas is initially inclined at an angle α_0 with respect to the shock plane. Effects of the initial column angle on the mixing characteristics are examined at Mach number 2.0 for column incline angles $1°$, $5°$, $10°$ and $30°$. Mean velocity profiles show that the column angle affects the gas velocity components in the vertical plane, but not in the spanwise direction. The gas undergoes higher initial upward acceleration at larger initial column incline angles. With time, the gas motion tends to become one-dimensional in the streamwise direction. Initially, velocity fluctuations are most intense within the interior of the column, but concentrate near the column leading edge over time. At high wavenumbers κ, the turbulent kinetic energy spectra follow a power-law scaling of κ^{-1}. The structure functions of the mass fraction do not clearly demonstrate power-law scaling except at early times for $\alpha_0 = 30°$, manifesting overall trends very similar to those observed in earlier experiments. Probability distributions of the mass fraction show independence of the mean and the standard deviation of the mixed gas on α_0. The column angle was also found to have little effect on the mixing efficiency characterized by the molecular mixedness. Velocity components in the streamwise and transverse directions tend towards a bimodal distribution for larger α_0.

Key words: turbulent mixing, shock waves

† Email address for correspondence: beromer@lanl.gov

B.E. Romero, J.M. Reisner, P. Vorobieff and S.V. Poroseva

1. Introduction

The Richtmyer–Meshkov instability (RMI) (Richtmyer 1960; Meshkov 1969) is generated when a shock passes through a perturbed interface separating two gases with different densities. The instability is formed by misalignment of the pressure gradient across the shock and the density gradient across the interface. This misalignment results in the formation of baroclinic vorticity, which then leads to the growth of perturbations at the interface, and mixing of the two gases (Brouillette 2002). As these perturbations grow, secondary, shear-driven instabilities develop, which cause smaller-scale mixing to occur (Vorobieff *et al.* 2004). See the review by Brouillette (2002) for a comprehensive description of the basic physical processes involved in the RMI. The recent reviews by Zhou (2017*a*,*b*) provide an extensive discussion on the applications, properties and analytical methods for flows exhibiting the RMI as well as the Rayleigh–Taylor and Kelvin–Helmholtz instabilities.

The process of shock-driven mixing by RMI occurs in flows at a range of scales. At the largest scales, shocks from supernova explosions propagate through gas and cosmic dust (Mendis & Rosenberg 1994; Woitke 2006; Bocchio, Jones & Slavin 2014), leading to formation of structures on the scale of light-years (Chevalier, Blondin & Emmering 1992; Kane, Drake & Remington 1999) and allowing for the creation of heavy elements. In contrast, inertial confinement fusion experiments produce flows on the scale of micrometres, where shock-driven mixing has the undesirable effect of dissipating energy, thereby reducing fuel compression and lowering fusion yield (Lindl, McCrory & Campbell 1992). The RMI can also be used to enhance the mixing of gaseous or liquid fuels in scramjet engines (Yang, Kubota & Zukoski 1993) and is essential for the operation of pulse detonation and rotating detonation engines (Huang *et al.* 2012).

Earlier experimental studies of the RMI have focused on the interaction of a planar shock with a single, sinusoidally perturbed interface (Meshkov 1969). Variations from this configuration include shock interactions with perturbed, planar interfaces such as those in the experiments of Rasmus *et al.* (2019) and V-shaped interfaces that were studied experimentally by Zhai *et al.* (2016). Experimental studies have also been conducted at the Atomic Weapons Establishment on the interaction of a shock with a finite-width interface featuring a 'chevron' shaped oblique perturbation by Smith *et al.* (2001), and of half-height interfaces by Holder & Barton (2004). The related numerical work by Hahn *et al.* (2011) studies the effect of additional perturbations on the oblique interfaces. These configurations are essentially two-dimensional (2-D), and the presence of the oblique interfaces leads to shock-driven deposition of vorticity on the interfaces, which leads to shear-driven instabilities.

Additional variations of the RMI include experiments conducted at Los Alamos National Labs, involving a shock interacting with one or more circular cylinders with their axes oriented parallel to the shock (Tomkins *et al.* 2003; Vorobieff *et al.* 2003, 2004; Kumar *et al.* 2005). These flow configurations do not feature shear-driven instabilities as their primary mechanism, but they do result in the formation of strong counter-rotating vortex pairs.

The variation of interest in this work has been studied in shock tube experiments at the University of New Mexico conducted by Olmstead *et al.* (2017*b*), which involved the interaction of a planar shock with an inclined circular cylinder of heavy gas. This study found that the RMI caused a counter-rotating vortex pair in the cross-sectional plane normal to the cylinder axis. However, on the column surface, it was discovered that the shock caused a Kelvin–Helmholtz instability (KHI) to form. This type of KHI, driven directly by the passage of the shock, has been named the shock-driven

KHI (SDKHI). Olmstead *et al.* (2017*b*) described an apparent correlation between the Mach number and the KHI wavelength, and proposed a scaling mechanism that could be used to compare experiments at various initial column angles. An additional study by Olmstead *et al.* (2017*a*) used the same experimental data to analyse structure functions of scalar intensity maps. The power-law scalings exhibited by these structure functions deviated from those proposed by the Obukhov–Corrsin and Kolmogorov theories (Sreenivasan 1996; Villermaux, Innocenti & Duplat 2001; Celani *et al.* 2005). However, in-depth characterization of the effects of the SDKHI on the transition to turbulence and mixing was not performed in the previous studies due to limitations of existing experimental techniques caused by the large range of scales involved and the impulsive nature of the RMI and SDKHI.

Popular experimental techniques used to study flows exhibiting RMI and SDKHI include planar laser-induced florescence (PLIF) and particle image velocimetry (PIV). These techniques present challenges to detailed studies of transition and mixing because they are limited to collecting data from a single plane at a given time. Certain important quantities, e.g. pressure fields, also cannot be measured. PLIF requires diluting the test gas with a suitable tracer and has limitations in quantifying planar velocity fields with velocimetry techniques (Palmer & Hanson 1994). PIV can provide velocity measurements but can suffer from particles not following the flow at high speed and interfering with the flow physics (Martins *et al.* 2021): adding tracer-like particles to shock-accelerated flow can produce shock-driven multiphase instability (Vorobieff *et al.* 2011), and may not capture fine-scale fluctuating velocities. The experimental studies of Olmstead *et al.* (2017*a*) in particular could not use PIV at higher Mach numbers due to both particle lag and seeding effects, and could not extract velocity fields using appropriate techniques specifically developed for PLIF, such as image correlation velocimetry (Tokumaru & Dimotakis 1995; Asay-Davis *et al.* 2009) because of insufficient temporal resolution.

Numerical simulations are often used to complement experimental studies by providing additional data inaccessible to experiments. Direct numerical simulations can produce detailed flow quantities at all scales of interest, but such simulations are still unfeasible for these types of flows due to their high computational costs. A more reasonable, commonly used alternative is large-eddy simulations (LES).

Applicability of LES to the flows with RMI was tested by Thornber, Groom & Youngs (2018), including comparison of the results obtained with different codes. The study found excellent agreement amongst all the codes at high grid resolutions for various considered flow characteristics. Tritschler *et al.* (2014) determined that gas composition in the mixing layer was predicted accurately with different LES approaches when compared to experiments. Some of the highest resolution LES of RMI to date have been conducted by Wong, Livescu & Lele (2019). In particular, they found that at late times, after re-shock, the flow resembled that of the Batchelor-type decaying turbulence. The early development of RMI was also considered in high-resolution simulations by Groom & Thornber (2019).

However, only a few simulations of RMI appearing in the shock–gas column interaction have been conducted previously (Palekar, Vorobieff & Truman 2007; Yang *et al.* 1993). These studies have mostly analysed large-scale flow features such as the interface width and the growth rate for 2-D circular gas clouds.

In our group, implicit LES (ILES) have been conducted for 2-D curtains (Romero *et al.* 2021*a*,*c*) and three-dimensional (3-D) heavy-gas columns (Romero *et al.* 2021*b*, 2022) to verify the mechanism leading to SDKHI and to analyse the effect of the flow dimensionality on the shock–column interaction. Simulations were run at Mach numbers ranging from 1.13 to 2.0. The gas curtains and columns were inclined at angles varying

from $10°$ to $45°$ with respect to the shock. The simulation results showed that the vorticity field produced by the shock after it passed through the gas column is consistent with a shear-driven flow, proving that the waves formed on the column surface were, in fact, Kelvin–Helmholtz waves. These wavelengths were found to be sensitive to the post-shock column diameter and were thus influenced implicitly by parameters such as the Mach number and the initial column/curtain angle. Furthermore, while SDKHI was observed to occur in both 2-D and 3-D simulations, 3-D effects were found to be important for the correct reproduction of the flow morphology and the interface growth rates seen in experiments.

The grid resolutions used in our previous simulations were not sufficient to conduct a detailed statistical characterization of the effects of SDKHI on transition to turbulence and mixing. The present study aims to overcome this limitation by conducting high-resolution ILES for the shock passing through a 3-D inclined cylindrical column of heavy gas. The simulation results are used to investigate the effect of SDKHI on the turbulent transition and mixing that occur in such a flow. In the simulations, a column of heavy gas (sulfur hexafluoride, SF$_6$) surrounded by air is inclined at a range of angles $\alpha_0 = 1°, 5°, 10°, 30°$ with respect to an oncoming shock with Mach number 2.0. The considered range of angles and the Mach number are chosen to facilitate comparison with the experiments of Olmstead *et al.* (2017*b*). The ensuing analysis compares mixing statistics with an emphasis on the mixing width and other integral mixing metrics. Energy spectra and anisotropy are also analysed for each case. In addition, scalar statistics in the vertical plane are compared to published experimental data to investigate the anomalous scaling reported by Olmstead *et al.* (2017*a*).

Simulations were performed with FIESTA, a graphics processing unit (GPU) accelerated flow solver developed at the University of New Mexico (Romero 2021) for multi-species compressible flows.

2. Numerical method and set-up

2.1. *Numerical method*

In this study, results were obtained using the 3-D, two-species, compressible, viscous transport equations in their conservative form. These equations consist of the continuity equations for each gas species, equations for each momentum component, and the conservation equation for specific total energy. The resulting system is represented by the following three equations:

$$\frac{\partial \rho Y_i}{\partial t} + \nabla \cdot (\rho \boldsymbol{u} Y_i) = 0, \tag{2.1}$$

$$\frac{\partial \rho \boldsymbol{u}}{\partial t} + \nabla \cdot (\rho \boldsymbol{u} \boldsymbol{u}^{\mathrm{T}} + p \boldsymbol{\delta}) = \nabla \cdot \boldsymbol{\tau}, \tag{2.2}$$

$$\frac{\partial \rho e_t}{\partial t} + \nabla \cdot \left[(\rho e_t + p) \boldsymbol{u} \right] = \nabla \cdot (\boldsymbol{\tau} \cdot \boldsymbol{u} - \boldsymbol{q}). \tag{2.3}$$

Here, ρ is the density of the mixture; Y_i is the mass fraction of species i, where Y_i is Y_a for air and Y_s for SF$_6$; $\boldsymbol{u}$ is the 3-D velocity vector $\boldsymbol{u} = [u_1, u_2, u_3]$, where 1, 2 and 3 are the streamwise (x), vertical (y) and spanwise (z) directions, respectively; p is the static pressure; e_t is the specific total energy; $\boldsymbol{\tau}$ is the viscous stress tensor; and $\boldsymbol{q}$ is the conductive heat flux vector.

The pressure of the gas mixture is computed with Dalton's mixing law (Dalton 1802) assuming ideal gas behaviour:

$$p = \rho \left(Y_s R_s T + (1 - Y_s) R_a T \right). \tag{2.4}$$

The mixture temperature is obtained from the internal energy as follows:

$$T = \frac{e}{C_{v_{mix}}}, \tag{2.5}$$

where e is the internal energy, and the mixture specific heat $C_{v_{mix}}$ is computed from the species specific heats and mass fractions as

$$C_{v_{mix}} = Y_s C_{v,s} + (1 - Y_s) C_{v,a}. \tag{2.6}$$

Expressions for the specific heats of individual species are

$$C_{v,a} = \frac{R_a}{\gamma_a - 1}, \quad C_{v,s} = \frac{R_s}{\gamma_s - 1}. \tag{2.7a,b}$$

The gas constants for each individual species are

$$R_a = \frac{R}{M_a}, \quad R_s = \frac{R}{M_s}, \tag{2.8a,b}$$

where R is the universal gas constant, M_a is the molecular weight of air, and M_s is the molecular weight of SF$_6$.

The viscous stress tensor $\boldsymbol{\tau}$ is

$$\boldsymbol{\tau} = 2\mu \boldsymbol{S} + \tfrac{1}{3} \mu \boldsymbol{\delta} (\nabla \cdot \boldsymbol{u}), \tag{2.9}$$

where μ is the mixture viscosity computed as $\mu = Y_a \mu_a + Y_s \mu_s$, and the strain rate tensor is given by

$$\boldsymbol{S} = \tfrac{1}{2} \left[\nabla \boldsymbol{u} + (\nabla \boldsymbol{u})^{\mathrm{T}} \right]. \tag{2.10}$$

Subsection 3.1 presents a detailed discussion of the relevant viscous and scalar dissipation length scales. Analysis of the results from the simulations indicates that the viscous length scales may be resolved partially by the grid, while length scales relevant to mass diffusion are not resolved. Therefore, the omission of mass diffusion terms in the governing equations presented above is appropriate for the flow regime under consideration.

The code solves fully dimensional equations. The specific values of parameters utilized in the code are $R = 8.314462$ J kg^{-1} mol^{-1}, $M_a = 0.028966$ kg mol^{-1}, $M_s = 0.14606$ kg mol^{-1}, $\mu_a = 2.928 \times 10^{-5}$ kg m^{-1} s^{-1}, $\mu_s = 1.610 \times 10^{-5}$ kg m^{-1} s^{-1}, $\gamma_a = 1.402$ and $\gamma_s = 1.092$.

Advective terms are approximated with the fifth-order weighted essentially non-oscillatory (WENO5) finite difference scheme (Jiang & Shu 1996; Ramani, Reisner & Shkoller 2019a,b). The pressure gradient term and the strain rate tensor are approximated using a fourth-order central difference scheme. The time scheme used is a low-storage, second-order, explicit Runge–Kutta integrator (Williamson 1980).
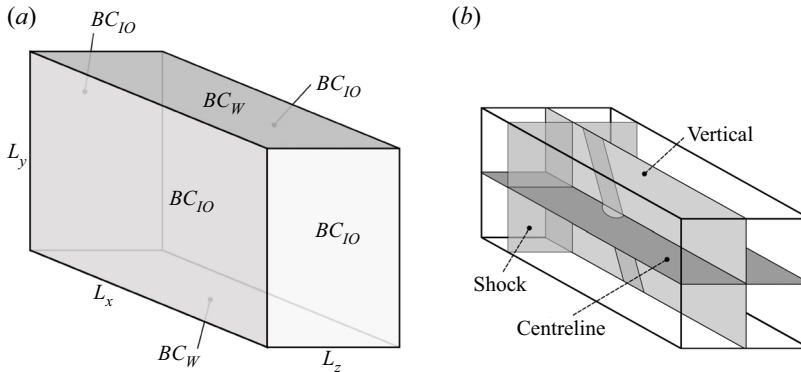
Figure 1. (*a*) Domain dimensions and boundary conditions for the inclined gas column simulations. (*b*) Illustration of the shock, the gas column, and the key cross-sectional planes.

2.2. *Computational domain and discretization*

Figure 1(*a*) depicts the computational domain used for the inclined gas column simulations. In the figure, $L_x = 0.4$ m is the length of the domain, $L_y = 0.08$ m is its height, and $L_z = 0.05$ m is its width.

The simulations used a uniform $10\,000 \times 2000 \times 1250$ Cartesian grid with $dx = dy = dz = 4.0 \times 10^{-5}$ m. This resolution exceeds that of the simulations of Palekar *et al.* (2007), and is similar to the values used in Wong *et al.* (2019) and Groom & Thornber (2019).

The time step $dt = 1 \times 10^{-8}$ s was chosen so that the CFL number, based on the maximum wave speed, did not exceed 0.1. Simulations were conducted for $80\,000$ time steps, which is equivalent to 0.8 ms, similar to the experiments of Olmstead *et al.* (2017*b*).

2.3. *Initial conditions*

Solution of (2.1)–(2.3) requires defining pre-shock and post-shock initial states. In this study, the pre-shock state was defined as atmospheric pressure and room temperature similar to the conditions observed in the experiments (Olmstead *et al.* 2017*b*). The post-shock conditions in air were determined from the inviscid normal shock relations for Mach number $M_0 = 2.0$. Table 1 lists the pre- and post-shock conditions used to initialize these simulations. Throughout this paper, post-shock quantities are indicated with the subscript '*post*' where necessary to remove ambiguity.

The gas column is positioned ahead of the shock at an angle α_0 to the shock, with the distribution of SF_6 mass fraction, Y_s, across the diameter of the gas column described by a Gaussian-based distribution with maximum concentration 1.0 at $x = x_0$: $Y_s = \exp[-(x - x_0)^2/2\sigma^2]$, where x_0 is the location of the centre of the cylindrical column. In experiments, steady-state initial conditions were established and well characterized (Wayne *et al.* 2015; Olmstead *et al.* 2017*a*,*b*), allowing value $\sigma = 1.71$ to be chosen so that the initial gas distribution used in the current simulations matched closely that seen in experiments. In the absence of well-characterized experimental initial conditions, or when steady-state initial conditions cannot be established experimentally, an alternative technique would be to pre-compute an appropriate interface, such as was done in the gas curtain experiments of Gowardhan & Grinstein (2011). The heavy-gas column diameter δ_0 is 10.4 mm as

971 A26-6

	Pre-shock	Post-shock
u_1	$0.0\ \mathrm{m\,s^{-1}}$	$0.0\ \mathrm{m\,s^{-1}}$
u_2	$0.0\ \mathrm{m\,s^{-1}}$	$434\ \mathrm{m\,s^{-1}}$
u_3	$0.0\ \mathrm{m\,s^{-1}}$	$0.0\ \mathrm{m\,s^{-1}}$
e_t	$2.14 \times 10^5\ \mathrm{J\,kg^{-1}}$	$4.56 \times 10^5\ \mathrm{J\,kg^{-1}}$
ρ	$1.16\ \mathrm{kg\,m^{-3}}$	$3.09\ \mathrm{kg\,m^{-3}}$
Y_a	1.0	1.0
Y_s	0.0	0.0

Table 1. Pre- and post-shock values for the initial conditions on the primary variables in (2.1)–(2.3).
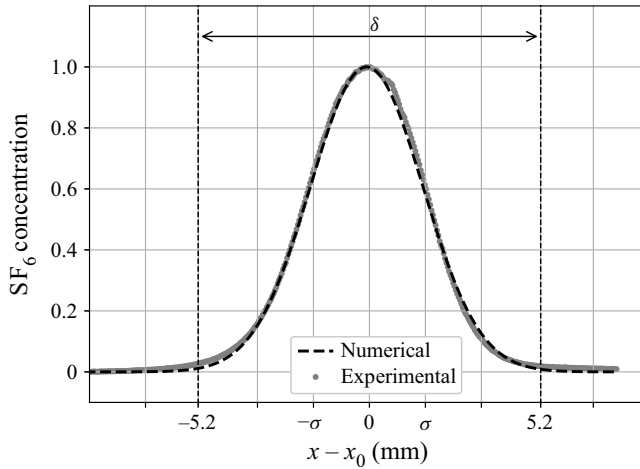
Figure 2. Comparison of the gas species distribution used in the simulations with the experimental data from Olmstead *et al.* (2017*b*). The location of the column diameter δ is indicated by vertical dashed lines.

measured at the location where the mass fraction of SF_6 has value 0.01. Figure 2 compares the gas distributions used in the simulations and in the experiments.

2.4. *Boundary conditions*

Boundary conditions for (2.1)–(2.3) include inflow/outflow boundaries (BC_{IO}) at $x = 0$, $x = L_x$, $z = 0$, $z = L_z$, and the reflective wall conditions (BC_W) at $y = 0$ and $y = L_y$ as seen in figure 1(*a*).

BC_{IO} conditions are defined as

$$\partial_x \rho(x, t) = 0, \quad \partial_x \rho\, u(x, t) = 0, \quad \partial_x \rho\, v(x, t) = 0, \quad \partial_x \rho\, e_t(x, t) = 0, \qquad (2.11a\text{–}d)$$

where $\partial_x = \partial/\partial x$ and $\partial_y = \partial/\partial y$.

BC_W conditions are defined as

$$\partial_y \rho(x, t) = 0, \quad \partial_y \rho\, u(x, t) = 0, \quad \rho\, v(x, t) = 0, \quad \partial_y \rho\, e_t(x, t) = 0. \qquad (2.12a\text{–}d)$$

3. Results

The initial density distribution in the domain is shown in figure 3 for the centreline and vertical planes (as defined in figure 1*a*). The green region to the left corresponds to the
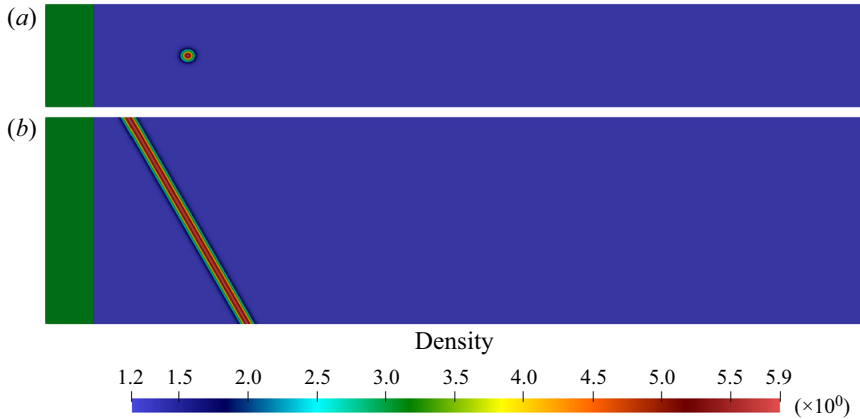
Figure 3. Initial conditions of the density in (*a*) the centreline plane and (*b*) the vertical plane used for simulations of a shock interacting with the gas column initially inclined at $\alpha_0 = 30°$.
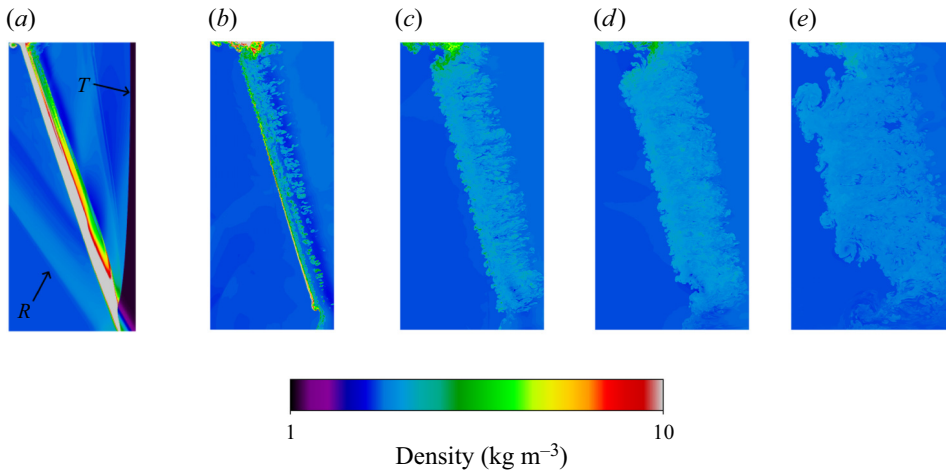

Figure 4. Density plots of the vertical plane at various dimensionless times τ for a Mach 2.0 shock interacting with an inclined circular column of heavy gas at initial angle $\alpha_0 = 30°$ to the plane of the shock. Arrows indicate the transmitted (T) and reflected (R) shocks. Times are (*a*) $\tau = 5.7$, (*b*) $\tau = 20.7$, (*c*) $\tau = 35.7$, (*d*) $\tau = 50.7$ and (*e*) $\tau = 110.8$.

shock wave and post-shock conditions, while the ambient, pre-shock conditions are seen in blue. Pressure is distributed uniformly within each of the two regions. The inclined gas column is seen to the right of the shock in the ambient region. The gas column is inclined at angle $\alpha_0 = 30°$ relative to the shock, similar to the experimental set-up used by Olmstead *et al.* (2017*b*).

As the simulation progresses, the shock travels to the right through the heavy-gas cylinder. Figures 4 and 5 depict the interaction of the shock with the cylinder at various times. The dimensionless time is defined as $\tau = \kappa A u_{post}(t - t_0)$ (Olmstead *et al.* 2017*b*). Here, $\kappa = 2\pi/\delta_0$ is the wavenumber based on the cylinder diameter in the experiments δ_0, $A = (\rho_{SF_6} - \rho_{air})/(\rho_{SF_6} + \rho_{air})$ is the Atwood number, u_{post} is the post-shock velocity, and t_0 is defined as the time when the shock interaction is halfway down the length of the initial column and corresponds to $\tau = 0$.
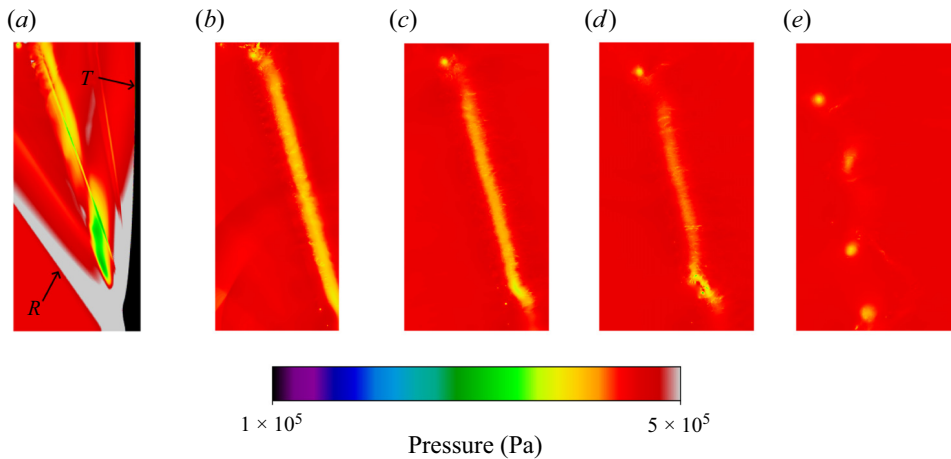
971 A26-8

Figure 5. Pressure plots of the vertical planes at various dimensionless times τ for a Mach 2.0 shock interacting with an inclined circular column of heavy gas at initial angle $\alpha_0 = 30°$ to the plane of the shock. Arrows indicate the transmitted (T) and reflected (R) shocks. Times are (a) $\tau = 5.7$, (b) $\tau = 20.7$, (c) $\tau = 35.7$, (d) $\tau = 50.7$ and (e) $\tau = 110.8$.

At $\tau = 5.7$, the shock has changed the inclination of most of the column to be $\alpha_{post} = 16.2°$. Due to differences in the density of the heavy gas and the air, the shock is refracted and bent inwards where it intersects the column (figures 4a and 5a). The shock becomes planar again after passing through the column. The column remains at this angle, $\alpha_{post} = 16.2°$, defined as the post-shock angle, for the remainder of its development.

High-pressure regions are seen behind the main shock and behind a reflected shock as seen in figure 5(a). These high-pressure regions intersect at the foot of the column and are likely to be responsible for an instability observed to form at the foot of the column. The instability is more evident by $\tau = 20.7$ (figure 4b). Similar phenomena were observed in 2-D simulations of SDKHI (Romero *et al.* 2021a). In the 3-D flow, this phenomenon still occurs, but is less pronounced.

After passage of the shock through the column, variations in the pressure field diminish until later times where pressure variations are coincident with spots of high vorticity.

The surface of the gas column begins to move upwards along its axis at $\tau = 20.7$. At a later time, $\tau = 35.7$, perturbations appear on the leading edge of the column. These perturbations first appear near the top of the column and progress quickly downwards towards the column foot. These perturbations are similar to the Kelvin–Helmholtz (KH) waves observed in the experiments of Olmstead *et al.* (2017b). In the experiments, the KH perturbations formed first on the column leading edge as they do in the 3-D simulations. The KH waves in 3-D simulations and in the experiments also have similar wavelengths and develop at the same times. The KH wavelengths λ_{KH} were identified by measuring the average distance between wave peaks. Wavelengths are well defined and have regular spacing for each column angle between $\tau = 20$ and $\tau = 25$ before additional secondary instabilities begin to appear. See Romero *et al.* (2022) for a detailed description of wavelength measurements and comparisons with experiments.

When results from the current 3-D simulations (figure 6a) are compared to those from the 2-D simulations of Romero *et al.* (2021a) (figure 6b), there are notable differences. The lengths of KH waves are much smaller in the 3-D case (table 2), and they form at first near the top of the column. In the 2-D case, the wavelengths are larger and
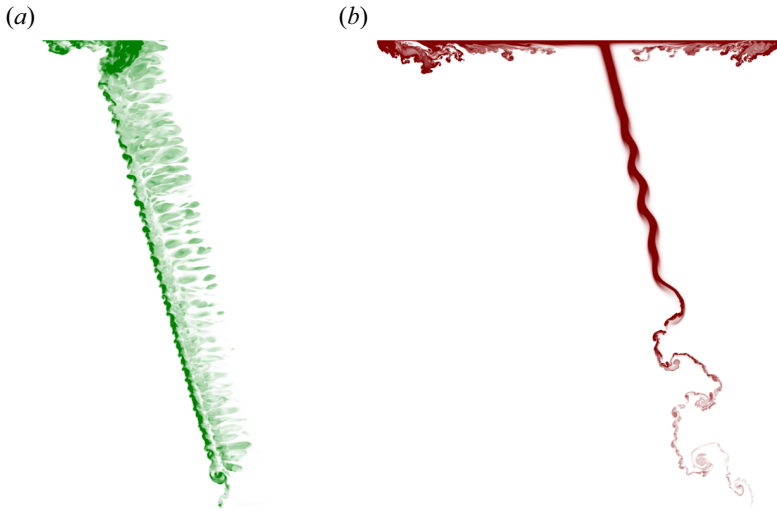
(*a*)   (*b*)

Figure 6. Comparison of the KH waves in the vertical plane of (*a*) the 3-D heavy-gas column at $\tau = 28.7$, and (*b*) a quasi-2-D heavy-gas curtain at $\tau = 73$ from Romero *et al.* (2021*a*).

	10°	20°	30°
2-D	1.41	1.49	1.65
3-D	0.066	0.092	0.168

Table 2. 2-D and 3-D average KH wavelengths normalized by pre-shock diameter λ_{KH}/δ_0 for different angles.

appear first near the column midpoint and at later times (figure 6*b*). The 3-D case also contains finger-like features downstream of the column. These features are caused by the counter-rotating vortex pair moving material into the vertical plane. Thus while 2-D simulations are important to emphasize or isolate certain flow features, 3-D simulations provide a more accurate description of the flow.

The turbulent state of the flow continues to evolve to $\tau = 50.7$. At later time $\tau = 110.8$, larger structures begin to dominate the flow.

Figure 7 depicts experimental results from Olmstead *et al.* (2017*b*). This image shows pixel intensity measurements collected with PLIF diagnostics of the gas column seeded with an acetone tracer; it can be compared to those in figure 4. In particular, the qualitative similarities near $\tau \approx 20$ and $\tau \approx 35$ are noted and show the similar timing of simulations with experiments.

Quantitative comparisons of KH wavelengths with experiments can be made using the wavelength selection mechanism introduced in Olmstead *et al.* (2017*b*):

$$\lambda_{KH} = D_C \tan(\alpha_2) \, M^{1/2} A^{1/2}, \tag{3.1}$$

where $D_C \propto \delta_0$ is the compressed column diameter defined in Olmstead *et al.* (2017*b*), α_2 is the post-shock angle of the column, M is the Mach number, and A is the Atwood number. Figure 8 compares mean wavelengths normalized by (3.1) for each column angle to mean wavelengths from experimental data. There is exceptional agreement at $\alpha_0 = 30°$ where
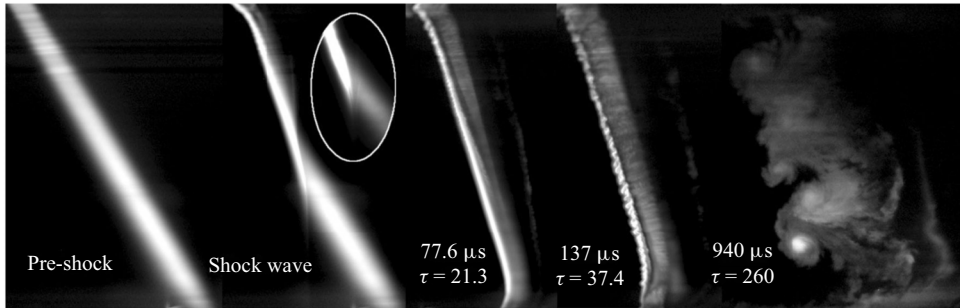
971 A26-10

Figure 7. Experimental data for a Mach 2.0 shock interacting with a cylindrical column of heavy gas with initial tilt angle 30°, reproduced with permission from Olmstead *et al.* (2017*b*).
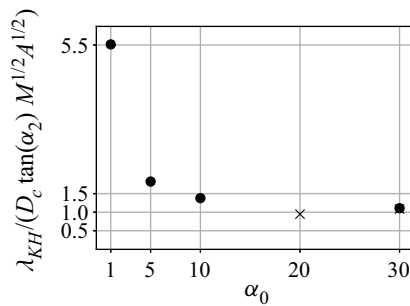

Figure 8. Normalized KH wavelengths at different angles for experiments ($\times$) and simulations ($\bullet$).

the data points overlap. However, this particular scaling does not seem to hold for smaller angles. For the cases $\alpha_0 = 1°$ and $\alpha_0 = 5°$, the wavelengths measured in simulations were identical and were resolved only by about five grid cells. This may indicate that the simulation resolution is insufficient to resolve the short wavelengths that occur at smaller initial tilt angles and is not necessarily a failing of the proposed wavelength selection mechanism. For detailed comparisons of simulations to experiment, see Romero *et al.* (2021*b*, 2022).

3.1. *Statistics*

Time averaging is not applicable in this flow to collect statistics for turbulence characterization. However, the central portion of the column appears to be homogeneous in the direction of the column tilt. This portion of the flow is used in the current study for collecting statistical data. Data are averaged at the vertical plane through the column axis and in the direction of the mean post-shock tilt angle of the column. For the analysis below, the flow field was cropped vertically to retain the centre third of the column. Horizontally, the domain was cropped to include the area where the SF_6 mass fraction first exceeds 0.001. Figure 9 shows the cropped flow field in the vertical plane for the 30° column at $\tau = 20.7$, along with an axis indicating the direction in which averages were taken.

Favre averaging (Favre *et al.* 1976) is used when extracting statistics. In this flow representation, the velocity field is decomposed into the mean and fluctuating components: $u_i = \widetilde{u}_i + u_i''$, where $\widetilde{u}_i = \langle \rho u_i \rangle / \langle \rho \rangle$ is the Favre-averaged mean velocity, and u_i'' is the
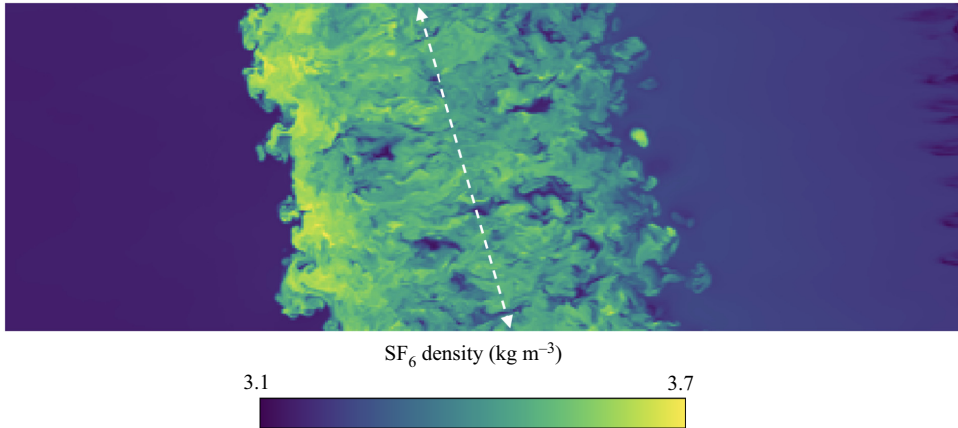
SF_6 density (kg m^{-3})

Figure 9. Vertical cross-section of the cropped density field for a 30° column used for collecting statistics at $\tau = 35.7$. The dashed line indicates the mean post-shock tilt angle along which averages were taken.

Favre-averaged velocity fluctuation. The spatial average of a variable ϕ is defined by

$$\langle \phi \rangle = \frac{1}{N} \sum_i \phi_i, \tag{3.2}$$

where N is the number of computational cells in the direction of the column tilt. For these simulations, $N = 650$ for the statistical region described above.

Below, data are presented with respect to the x-coordinate normalized as

$$x^*(y) = \frac{x - x_0(y)}{w}, \tag{3.3}$$

where $x_0(y)$ is the location of the leading edge of the column and depends on the y-coordinate due to the post-shock angle, and w is the width of the column defined by the locations at the leading and trailing edges where the mass fraction is 0.001.

Profiles of the mean mass fraction $\langle Y_s \rangle$ and of the mean velocity components $\widetilde{u}_i$ were computed at different times in the streamwise direction and are shown in figure 10. In the figure, the mean velocity components are normalized by the post-shock velocity u_{post}.

Figure 10(*a*) shows that at early time, the concentration of SF_6 is highest on the leading edge. As time progresses, the SF_6 concentration becomes more uniform inside the column.

Figures 10(*b*)–10(*d*) show that the flow motion in the vertical plane of the gas column occurs mainly in the x- and y-directions. In the streamwise direction, the shock accelerates the gas near the edges of the column to a higher velocity than the gas in the interior of the column. With time, the minimum value of u_1 moves within the column, finally localizing between the column centre and the leading edge, as shown in figure 10(*b*) at $\tau = 50.7$. After that time, the profile of this velocity component tends to the post-shock velocity (the value 1.0 in figure 10*b*) at all locations (not shown here).

In the y-direction, the gas column inclination causes the dense gas to accelerate upwards almost everywhere through the column width (figure 10*c*). The less dense gas at the column edges moves downwards. As time progresses, the dense gas motion in the area between the column centre and its trailing edge reverses its direction, with all gas moving downwards. At $\tau = 20.7$, only the gas near the leading edge is still moving upwards. By $\tau = 50.7$, there is almost no gas motion in the vertical direction.
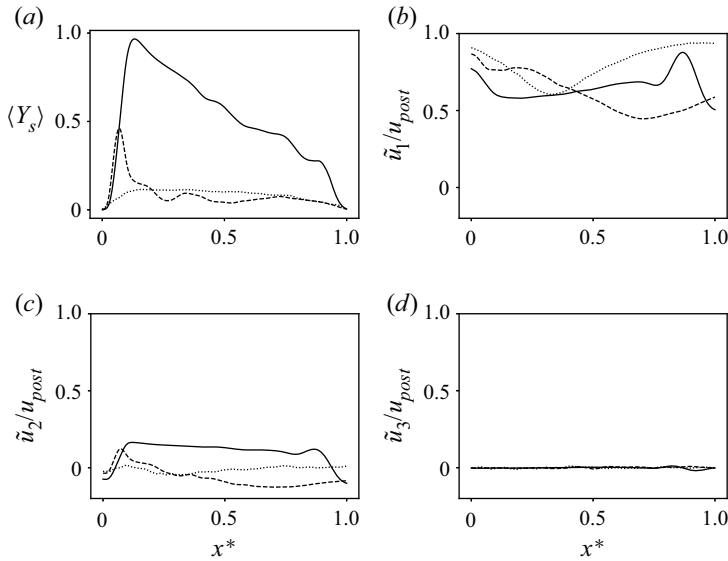
Figure 10. Mean mass fraction and mean velocity profiles for a column with initial tilt $\alpha_0 = 30°$ at different times τ: 5.7 (solid line), 20.7 (dashed line), and 50.7 (dotted line).
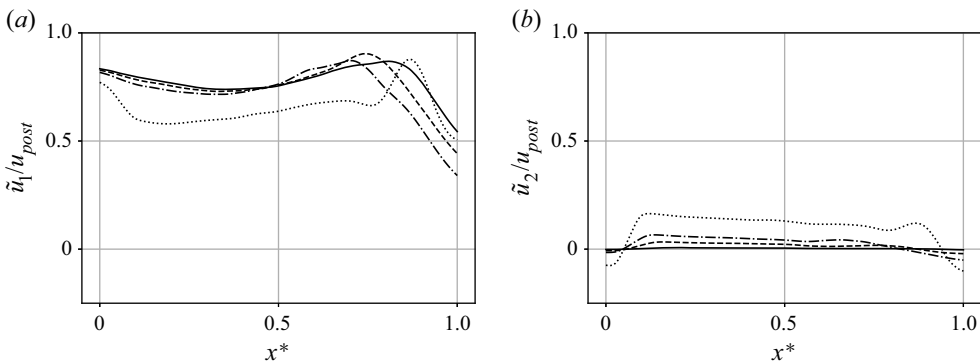

Figure 11. Mean (a) x-velocity and (b) y-velocity at $\tau \approx 5.7$ for columns with different initial angles: $1°$ (solid line), $5°$ (dashed line), $10°$ (dash-dotted line), and $30°$ (dotted line).

The velocity in the z-direction, u_3, is close to zero at all locations within the column and at all times (figure 10d). This is due to the column cross-sectional symmetry being preserved with time for the chosen sample plane.

The column inclination angle was found to affect the gas x- and y-velocity components (figure 11), but not the velocity component in the z-direction. Specifically, in the x-direction, columns with initial angles up to $\alpha_0 = 10°$ have similar profiles (figure 11a). The gas is accelerated mostly at the column leading edge and in an area behind the trailing edge. At angle $30°$, the areas of high gas velocity are more narrow, with the second peak shifting closer to the column trailing edge. At any column angle, the gas at the trailing edge accelerates less than the rest of the column when experiencing a shock.

In the y-direction, the gas was found to accelerate upwards to a higher velocity for larger initial angles α_1, as shown in figure 11(b). At any angle, the gas velocity in the y-direction is less than in the x-direction.
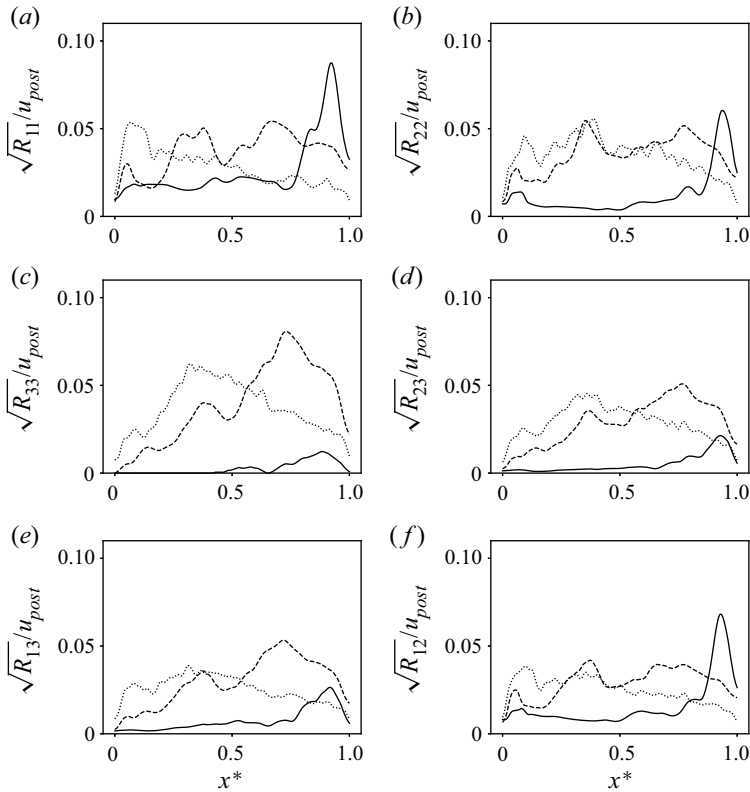
Figure 12. Evolution of the Reynolds stresses with time for a column with initial tilt $\alpha_0 = 30°$ at different times τ: 5.7 (solid line), 20.7 (dashed line), and 50.7 (dotted line).

Overall, we can infer that the gas motion in such a flow geometry is mainly 2-D in the vertical plane, and with time becomes predominantly one-dimensional (in the x-direction).

Normalized Reynolds stresses are presented in figure 12 as $\sqrt{R_{ii}}/u_{post}$, where the Favre-averaged Reynolds stresses are defined as

$$R_{ij} = \frac{\left\langle \rho u_i'' u_j'' \right\rangle}{\langle \rho \rangle}. \tag{3.4}$$

These figures show that initially, the intensities of all fluctuating velocities and of the shear stresses have a maximum near the trailing edge of the column. Over time, the peak values of all Reynolds stresses move towards the leading edge of the column ($x^* = 0$), with stresses generally growing in time across the entire column.

The Reynolds number describing this flow must be defined using the most physically relevant velocity and length scales. The flow features observed and characterized in this work evolve after the shock interaction with the density interface produces baroclinic vorticity. Therefore, neither the piston velocity of the shocked flow nor the shock front speed are relevant – the patterns observed are produced by the fluctuating components of the velocity field due to the deposition of baroclinic vorticity. Here, this characteristic velocity is represented by the average magnitude of fluctuating velocity, $u_{turb} = \sqrt{R_{11} + R_{22} + R_{33}}$. The appropriate length scale can be determined from the same considerations. According to Richtmyer (1960), the initial (linearized) perturbation

amplitude growth $a(t)$ is proportional to the instability wavenumber κ and to the initial instability amplitude. For a fixed amplitude, the instability growth is faster for higher wavenumbers (and smaller wavelengths). The feature that is associated with the highest initial amplitude and the lowest wavelength in the centreline plane is the heavy-gas column diameter δ_0, and in the vertical plane it is the KH wavelength λ_{KH} (which is related to δ_0 via (3.1)).

For the cases considered, the characteristic velocity is $u_{turb} = 65.1$ m s^{-1}, the mean post-shock density is $\rho_{post} = 3.6$ kg m^{-3}, and the mean mixture viscosity is $\mu_{mix} = 2.65 \times 10^{-5}$ kg m^{-1} s^{-1}. For the characteristic length δ_0, the Reynolds number $Re_\delta = \rho_{mix} u_{turb} \delta_0 / \mu_{mix}$ can be estimated as $\sim$90 000. This is perhaps the most realistic estimate, because it is associated with the scale that also produces the strongest vorticity deposition in the form of counter-rotating vortex pairs in the centreline plane. In direct experimental measurements of the flow field in a similar geometry (periodically perturbed gas curtain with wavelength $\lambda = 6$ mm) but at an appreciably lower Mach number 1.2, the Reynolds number varied in the range $10\,000 < Re < 22\,500$ (Prestridge *et al.* 2000).

However, the present study is concerned with the flow evolution in the vertical plane, so the scale λ_{KH}, varying in our simulations from 0.66 mm to 1.68 mm, becomes relevant. An estimate for the Reynolds number based on such a length scale, $Re_\lambda = \rho_{mix} u_{turb} \lambda_{KH} / \mu_{mix}$, is in the range between 6000 and 17 000.

Information about the Reynolds number range can be used further to estimate characteristic length scales for viscous and mass diffusion processes. For viscous processes, the Taylor and Kolmogorov length scales can be approximated by $\lambda_T = \lambda_{KH} Re_{\lambda_{KH}}^{-1/2}$ and $\eta = \lambda_{KH} Re_{\lambda_{KH}}^{-3/4}$, where λ_T is the Taylor microscale, and η is the Kolmogorov microscale. For the range of Reynolds numbers $Re_{\lambda_{KH}}$ identified above (going with the more conservative estimate), this results in $\lambda_T = 10\,\mu$m to $40\,\mu$m, and $\eta = 1\,\mu$m to $10\,\mu$m. The grid spacing is d$x = 40\,\mu$m, which indicates that the viscous dissipation range may be partially resolved, so viscous effects must be accounted for.

The scalar dissipation length scale is relevant to the mass diffusion process and can be computed as $\eta_D = \eta Sc^{-3/4}$, where Sc is the Schmidt number (Sreenivasan 2019). The Schmidt number is defined as $Sc = \mu_{mix}/(\rho_{mix} D)$, where $D = 2.23 \times 10^{-6}$ m^2 s^{-1} is the mean diffusion coefficient between air and SF$_6$ at the post-shock temperature and pressure, resulting in $Sc = 2.8$. These estimates give a range for the mass diffusion length scale η_D between $0.5\,\mu$m and $5\,\mu$m. This is smaller than the grid resolution d$x = 40\,\mu$m, so the length scales at which mass diffusion processes occur are not resolved. Notably, the Péclet number $Pe = Sc Re_{\lambda_{KH}}$ ranges from 17 000 to 48 000, which is much larger than unity, indicating that the effects of mass diffusion occur on a significantly larger time scale than those of the advective transport. For these reasons, the effects of mass diffusion are not included in this study and can be disregarded safely on the time scales of interest.

3.2. *Anisotropy*

In this subsection, the flow anisotropy is studied. For this purpose, the anisotropy tensor is defined as

$$b_{ij} = \frac{R_{ij}}{R_{kk}} - \frac{1}{3}\,\delta_{ij}, \tag{3.5}$$

where δ_{ij} is the Kronecker delta, and R_{ij} is the Favre-averaged Reynolds stress tensor defined above.
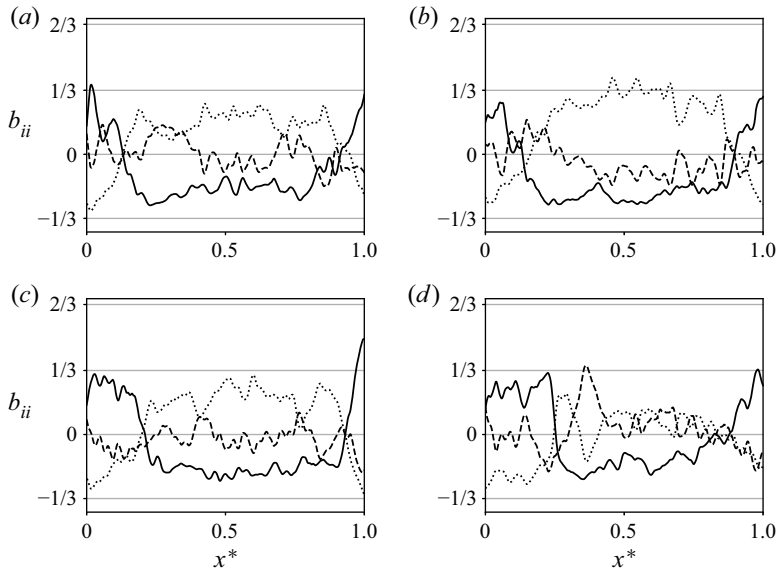
Figure 13. Anisotropic tensor components for columns with initial angles (*a*) $1°$, (*b*) $5°$, (*c*) $10°$ and (*d*) $30°$. The components are b_{11} (solid line), b_{22} (dashed line) and b_{33} (dotted line).

The diagonal components of the anisotropy tensor give an estimate of the contribution of each fluctuating velocity component to turbulent kinetic energy. These values range from $-1/3$, corresponding to zero energy from that component, to $2/3$, corresponding to all energy coming from that component. If all three diagonal components of the anisotropy tensor b_{ij} are zero, then the flow is isotropic.

Figure 13 shows diagonal components of the anisotropy tensor for different initial column angles at approximately the same time $\tau = 85.1$. Turbulent energy is distributed non-uniformly through the column at each angle. For the smaller angles ($\leq 10°$), the flow is anisotropic throughout, dominated by the streamwise velocity fluctuations near the leading and trailing edges of the column, and by the spanwise fluctuations in the column interior. For the $30°$ column, the flow becomes more isotropic in the interior of the column, with the transverse and vertical fluctuations having equal contributions to turbulent kinetic energy.

In addition to examining the components, invariants of the anisotropy tensor can be plotted to examine the turbulence state over time. The anisotropy tensor invariants η and ξ are defined as

$$6\eta^2 = b_{ij}b_{ji}, \tag{3.6}$$

$$6\xi^3 = b_{ij}b_{jk}b_{ki}, \tag{3.7}$$

where b is the anisotropy tensor defined in (3.5), and repeated indices indicate summation. For realizable turbulence, η and ξ fall within the Lumley triangle, with the sides and vertices of the triangle representing special states of the Reynolds stress tensor (Pope 2000).

Anisotropy-invariant maps are plotted for each column initial angle in figure 14. Figure 14(*a*) provides an overview of the Lumley triangle with an invariant map at three locations ($x^* = 0.1, 0.5, 0.9$) within the $30°$ column. For all cases, the trajectories are contained within only a small portion of the Lumley triangle, so figures 14(*b–e*) are
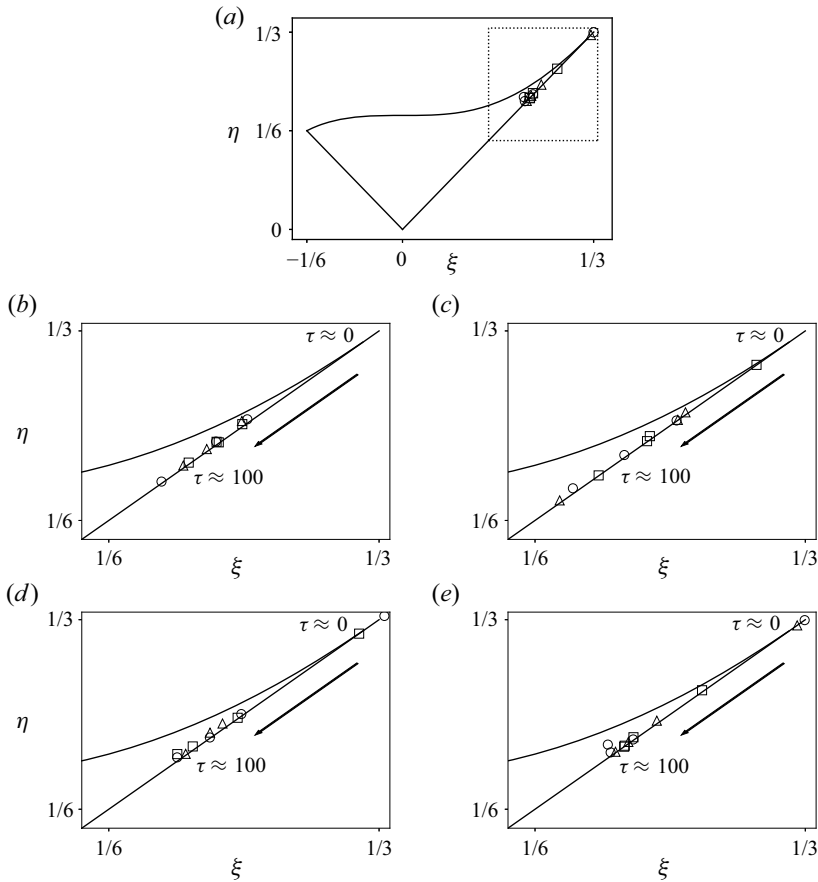
971 A26-16

Figure 14. Reynolds-stress-invariant maps with (*a*) an overview of the Lumley triangle and (*b*–*e*) columns with different initial angles for three locations within the column: (*b*) $1°$, (*c*) $5°$, (*d*) $10°$ and (*e*) $30°$. Circles indicate $x^* = 0.1$, triangles indicate $x^* = 0.5$, and squares indicate $x^* = 0.9$.

restricted to the region indicated by the dotted box in figure 14(*a*). Arrows indicate the direction of the invariant trajectories with time.

For each case, the initial values of η and ξ are near the limit of single-component turbulence as fluctuations are initially present in only the *x*-direction (figure 13). As time progresses, the flow behaviour changes in the direction of isotropy while maintaining a state close to that of axisymmetric turbulence.

3.3. *Mixedness*

The molecular mixedness ratio over time can also be compared for columns with different initial angles. In the current study, molecular mixedness is defined as

$$\theta = \frac{\langle \chi_s (1 - \chi_s) \rangle_V}{\langle \chi_s \rangle_V \langle (1 - \chi_s) \rangle_V}, \tag{3.8}$$

where $\langle \cdot \rangle_V$ is the volumetric mean defined below, and χ_s is the mole fraction of SF_6. The mole fraction is given by $\chi_s = n_s/(n_s + n_a)$, where $n_i = \rho Y_i/M_i$ is the molar count of species *i* in a given grid cell with mass fraction Y_i and molecular mass M_i. The volumetric
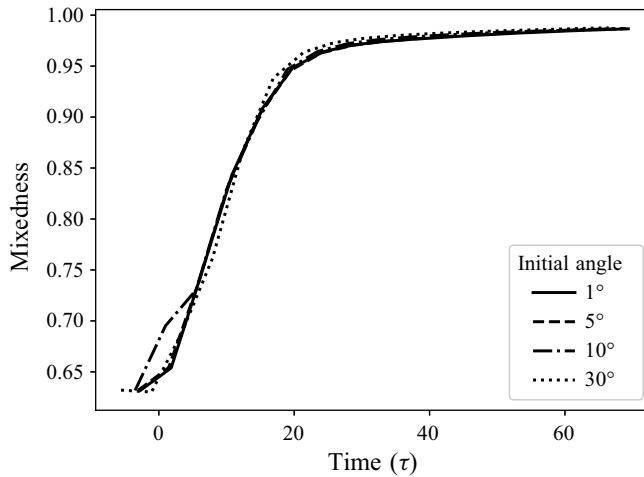
Figure 15. Volume mean molecular mixedness ratio of SF_6 over time for different initial column angles.

mean is defined as

$$\langle \phi \rangle_V = \frac{1}{N_x N_y N_z} \sum_i \sum_j \sum_k \phi_{ijk}, \tag{3.9}$$

where N_x, N_y and N_z are the numbers of grid cells in the x-, y- and z-directions, respectively, and ϕ_{ijk} is the value at the grid cell with coordinates (i, j, k).

A value $\theta = 1$ means that the flow is mixed as much as possible within the volume, which means that the SF_6 is distributed uniformly.

Figure 15 shows the molecular mixedness ratio over time for different initial column angles. For each angle, the column has initial molecular mixedness $\theta = 0.62$ due to the diffuse interface across the column defined by the initial conditions (see figure 2). Over time, the mixedness tends to value 1 for each initial angle, while the initial angle has very little effect on the mixing rate. At times beyond $\tau = 60$, large-scale structures begin to impact the statistical region, and this may affect the mixedness behaviour. The apparent deviation for the $10°$ column near $\tau \approx 0$ is a numerical artefact due to the presence of the shock wave within the statistical region under consideration that happens in this particular case. The shock is not parallel to the column tilt angle and disrupts the averaging procedure in (3.8). In other cases, solution data files do not capture the shock wave within the statistical region due to the I/O frequency of the simulation.

3.4. *Spectra*

Figure 16 shows energy spectra at different times for heavy-gas columns with various initial tilt angles. Here, spectral energy is defined as $E = \left\langle \frac{1}{2} \hat{v}_i^* \hat{v}_i \right\rangle$, where $v_i = \sqrt{\rho} \, u_i''$, $(\hat{\cdot})$ is the one-dimensional Fourier transform in the homogeneous direction, and $(\cdot)^*$ is the complex conjugate. The non-dimensional time τ depends on t_0, which itself depends on initial tilt angle α_0. Simulation data files may not capture t_0 exactly for each angle, resulting in slightly different values of τ for each solution file set, so spectra for different initial column angles are compared at close, but non-equal times.

At every angle, an apparent power-law scaling may be observed between wavenumbers $\kappa = 30$ and $\kappa = 100$ (indicated by the arrows in figure 16). These wavenumbers
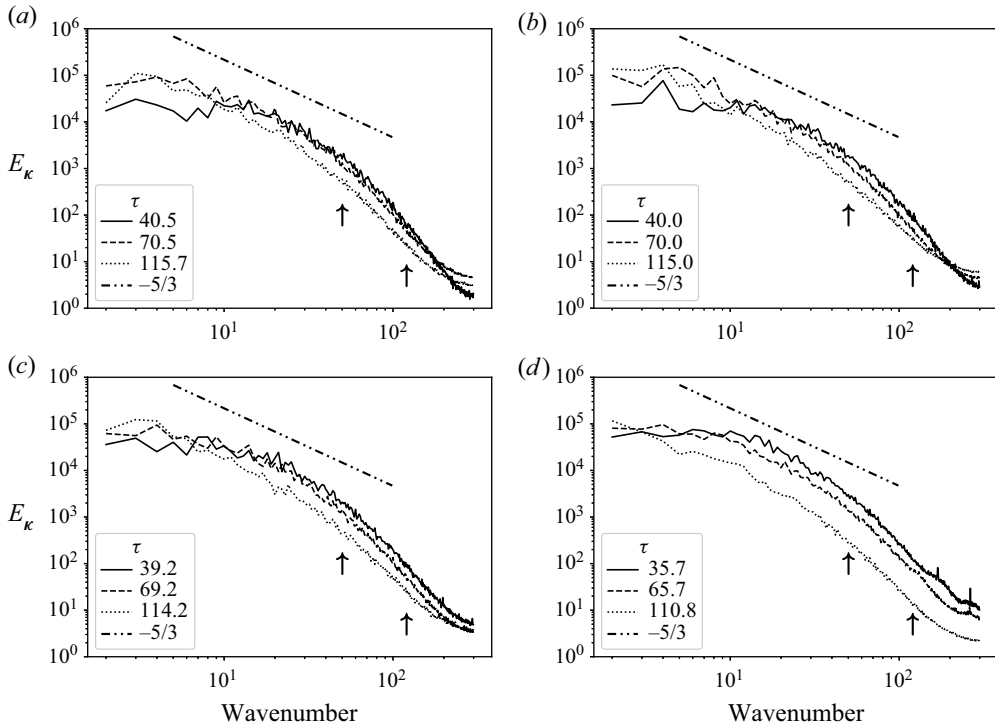
971 A26-18

Figure 16. Mean turbulent kinetic energy spectra in the vertical plane at different times for columns with initial angles (*a*) $1°$, (*b*) $5°$, (*c*) $10°$ and (*d*) $30°$.

τ	$1°$	$5°$	$10°$	$30°$
35.7	-1.01	-1.05	-1.04	-0.98
65.7	-0.94	-0.98	-1.01	-0.93
110.8	-0.88	-0.85	-0.96	-0.90

Table 3. Energy spectra power-law exponents at different times for different initial column angles.

correspond to length scales 0.4 mm and 0.12 mm, respectively. The values for the power-law exponent p were computed by fitting a line through the apparent power-law region of the energy spectra. These values are presented in table 3. These power-law exponents are all close to -1 at early times, but decrease slightly in magnitude over time for all considered angles. These values are in agreement with the power-law scalings observed by Olmstead *et al.* (2017*a*) for scalar structure functions. In ideal Kolmogorov turbulence, exponents of the energy spectrum and the spectrum of a diffusive scalar (passive or even reactive) should be equal, provided that the same conditions are met as those necessary for the equivalence between spectral and structure function representation of the flow (Monin & Yaglom 2013).

3.5. *Structure functions*

To examine further the power-law behaviour of this flow, second-order, scalar structure functions were assembled for the SF_6 mass fraction in a manner similar to those presented
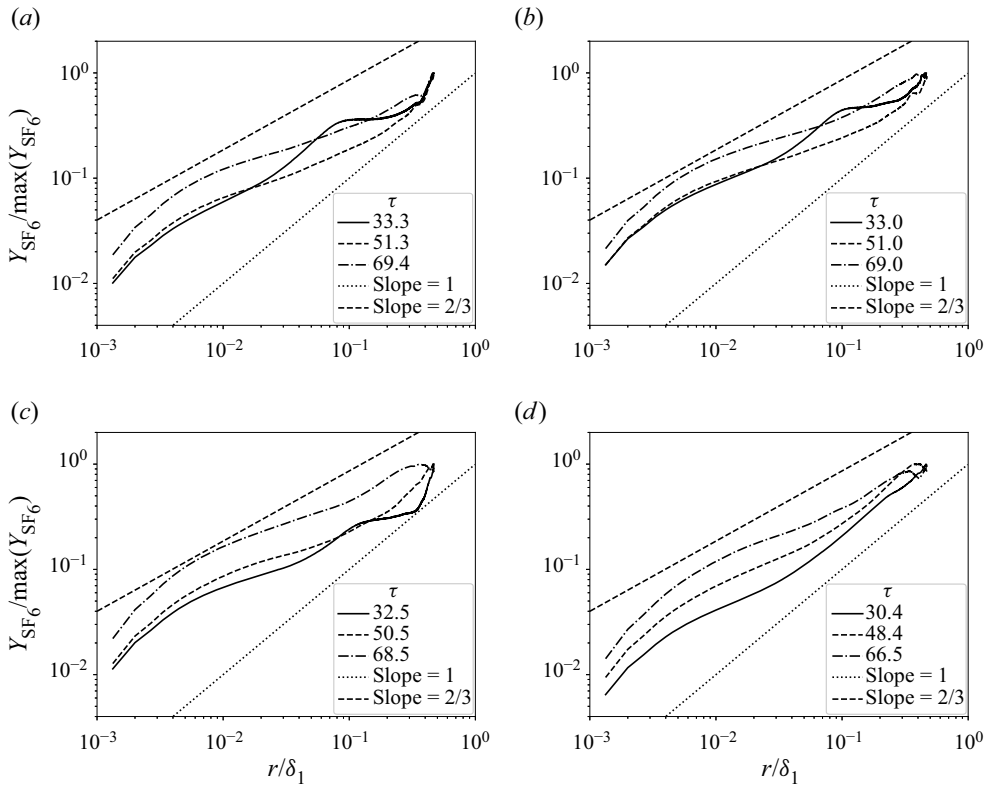
Figure 17. Structure functions of mass fraction at various initial inclination angles: (*a*) $\alpha_0 = 1°$, (*b*) $\alpha_0 = 5°$, (*c*) $\alpha_0 = 10°$ and (*d*) $\alpha_0 = 30°$.

in Olmstead *et al.* (2017*a*):

$$Y_{s2}(r) = \left\langle [Y_s(\boldsymbol{x}) - Y_s(\boldsymbol{x} + \boldsymbol{r})]^2 \right\rangle, \tag{3.10}$$

where $r = |\boldsymbol{r}|$ is the magnitude of radius vector $\boldsymbol{r}$, and $\langle \cdot \rangle$ denotes averaging over all pairs of points in the same region as the statistics defined previously. The structure function computations have quadratic efficiency, $O(n^2)$, and can be prohibitively costly for high-resolution datasets. An algorithm was developed for the current study to produce structure function data that utilized the Kokkos framework (Edwards, Trott & Sunderland 2014) to take advantage of the performance benefits of GPU systems.

Structure functions evolving in time are shown in figure 17 for different initial gas column angles. For reference purposes, two lines are added to each plot: one corresponds to the power-law exponent 2/3 that is expected theoretically in homogeneous isotropic turbulence (Celani *et al.* 2005; Monin & Yaglom 2013), and the other corresponds to the power law with the exponent close to unity observed in some experimental runs of Olmstead *et al.* (2017*a*). As the figure demonstrates, numerical results resemble a power law with the exponent close to unity only at the inclination angle $\alpha_0 = 30°$ at early times, and for large scales only. There is no single power-law exponent fitting all scales at any given inclination angle at any time. Overall, the results are remarkably similar to the experiment (figure 3 of Olmstead *et al.* 2017*a*): the plots can be interpreted as showing

971 A26-20

the transfer of energy from large scales (here, the integral scale would be related to the geometry of the initial conditions – representative gas column size after compression) to small scales, but an inertial range spanning multiple orders of magnitude does not develop.

This is not surprising as, strictly speaking, this flow is transitioning to turbulence (at least in the phenomenological sense) in a non-canonical case that is distinct from the homogeneous, isotropic, fully developed classical Kolmogorov turbulence.

First, the entire energy input driving the turbulent transition is provided by the shock interaction with density interfaces over a finite time. Accordingly, the spectral properties of kinetic energy fluctuations in RMI-driven mixing differ from those of Kolmogorov turbulence (Abarzhi & Sreenivasan 2022).

Second, it is important how the flow is driven on the injection scale. For the flows considered here, a reasonable assumption is that the driver is shear on several scales (dictated by the initial conditions geometry) due to RMI. A recent theory of shear-driven turbulence suggests that the second-order velocity structure function is affected by both the isotropic ($r^{2/3}$) and non-isotropic ($r^{4/3}$) contributions (Kumar, Meneveau & Eyink 2022), whose respective roles may also be scale- and time-dependent. This could explain some of the behaviours observed in figure 17. A different way to look at decaying turbulence involves considering how the effective length scale varies with time, producing an unsteady cascade (Goto & Vassilicos 2016). A somewhat similar approach in an earlier theory (George 1992) considers the possibility that a universal scaling for spectra may exist not for the wavenumber κ, but for a different object (κl, where l is the time-dependent length scale, in the George theory). The best theoretical approach to the flow considered in this work could be one taking into consideration the influence of the initial conditions (irrelevant for the fully developed turbulence case) on scalings. Whether the turbulence is affected by how it is driven in time, in space, or both, the appearance of the spectra (in terms of κ) or structure functions (r) may change.

Third, there is the possibility of a mismatch between numerics and experiment due to diagnostics. In experimental PLIF results, imaging shows the laser-induced fluorescence intensity from the tracer gas that usually closely follows mass concentration; however, possibilities for several diagnostic-related discrepancies remain (Melton & Lipp 2003). An example of such a discrepancy is discussed in § 3.6. Some subtler differences between experiment and numerics could also be attributable to differences in initial conditions: in the experiments, the diffuse gas column always has small perturbations that the numerical initial conditions do not attempt to reproduce. In a sense, this would mean that in the experiments, there is an additional initial contribution to disorder in the flow.

For possible future studies, it might be worthwhile to consider the approach described by Vorobieff *et al.* (2003), where ensembles of velocity fields from multiple experimental realizations were collected for the same experiment with nominally identical initial conditions. This made it possible to produce ensemble-averaged velocities and then extract velocity fluctuation fields for each individual experiment. Notably, while the structure functions for the full velocity fields manifested steeper slopes, the fluctuation field slopes were closer to 2/3. In numerics, small fluctuations could be added to the initial conditions to produce similar ensembles (Palekar *et al.* 2007).

3.6. *Probability density functions*

In this subsection, we present probability density functions (p.d.f.s) for mass fraction, vorticity components and velocity components in order to further characterize the flow development.
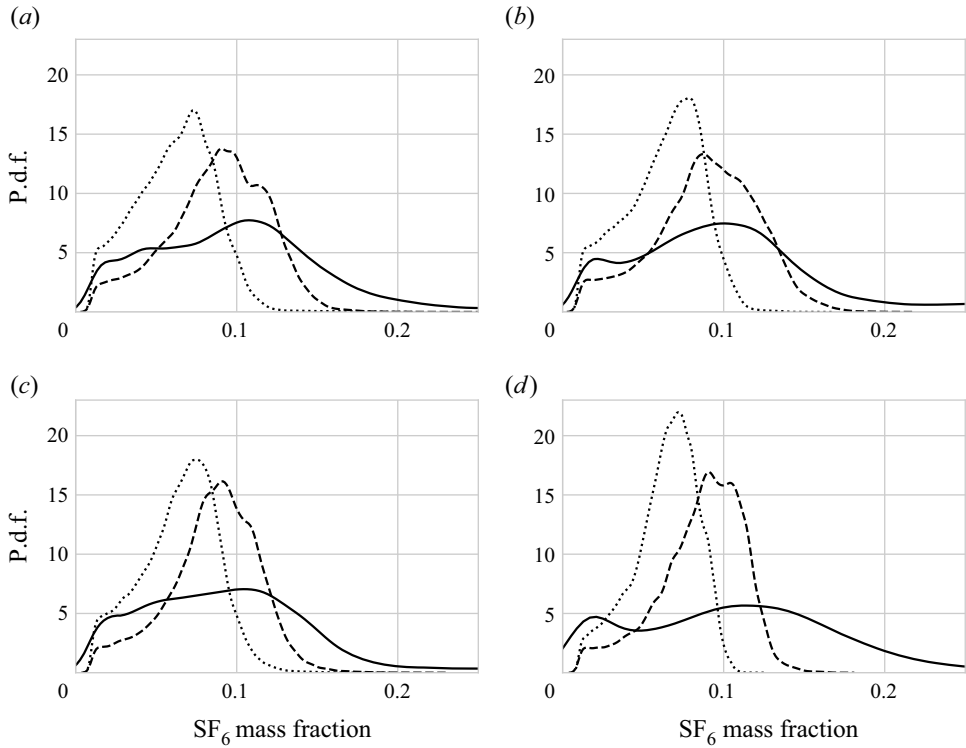
Figure 18. P.d.f.s of SF_6 mass fraction Y_s for columns with different initial tilt angles α_0, at different times τ: 5.7 (solid line), 35.7 (dashed line), and 110.8 (dotted line). Angles are (*a*) $1°$, (*b*) $5°$, (*c*) $10°$ and (*d*) $30°$.

To construct discrete p.d.f.s, a bin size is defined to be $\Delta\phi = (\phi_{max} - \phi_{min})/N_b$ for some quantity ϕ, where N_b is the number of bins. A bin count $N_b = 96$ was selected to produce smooth p.d.f. profiles with an adequate number of samples within each bin. Values of ϕ are then distributed into the N_b bins, yielding the sample count of N_k per bin. The p.d.f. is then defined by $P(\phi) = N_k/\Delta\phi N$, where N is the total number of samples of ϕ. This definition results in $\sum_{k=1}^{N_k} P(\phi)\,\Delta\phi = 1$.

The p.d.f.s of the SF_6 mass fraction Y_s (figure 18) were constructed using the mass fraction data from the same region as the statistics discussed in previous subsections. That is, the vertical cross-section is cropped vertically to retain the central one-third of the column using $Y_s = 0.001$ as a criterion to determine the upstream and downstream edges of the column. Within this region, Y_s falls between 0.0 and 0.27 at all times for each initial tilt angle.

At early times, immediately after passage of the shock, lower values of the mass fraction (≈ 0.0–0.15) are approximately equally likely at all tilt angles of the gas column, while the probability of higher mass fractions decreases rapidly (figures 18*a*–*d*). At later times, the p.d.f.s take on a bell-like shape. Tables 4(*a*)–4(*d*) present the mean, standard deviation (SD), skewness and kurtosis over time for each initial column angle. These values were computed using the mean(), std(), skewness() and kurtosis() subroutines from the pandas Python library (pandas development team 2020).

With time, the distribution becomes more narrow at all considered column angles. The mean, corresponding to the peak of the distribution, decreases with time for all initial

971 A26-22

τ	Mean	SD	Skewness	Kurtosis	τ	Mean	SD	Skewness	Kurtosis
5.7	0.106	0.066	1.463	3.647	5.7	0.111	0.075	1.461	2.499
35.7	0.087	0.031	−0.310	−0.218	35.7	0.089	0.032	−0.269	−0.194
110.8	0.061	0.025	0.094	0.283	110.8	0.063	0.024	−0.323	−0.553

(a) 1°   (b) 5°

τ	Mean	SD	Skewness	Kurtosis	τ	Mean	SD	Skewness	Kurtosis
5.7	0.107	0.077	1.805	3.828	5.7	0.133	0.121	2.516	7.612
35.7	0.085	0.028	−0.359	0.170	35.7	0.086	0.026	−0.654	0.189
110.8	0.064	0.024	−0.186	−0.187	110.8	0.064	0.019	−0.567	−0.153

(c) 10°   (d) 30°

Table 4. Mass fraction p.d.f. statistics over time for different initial column angles.
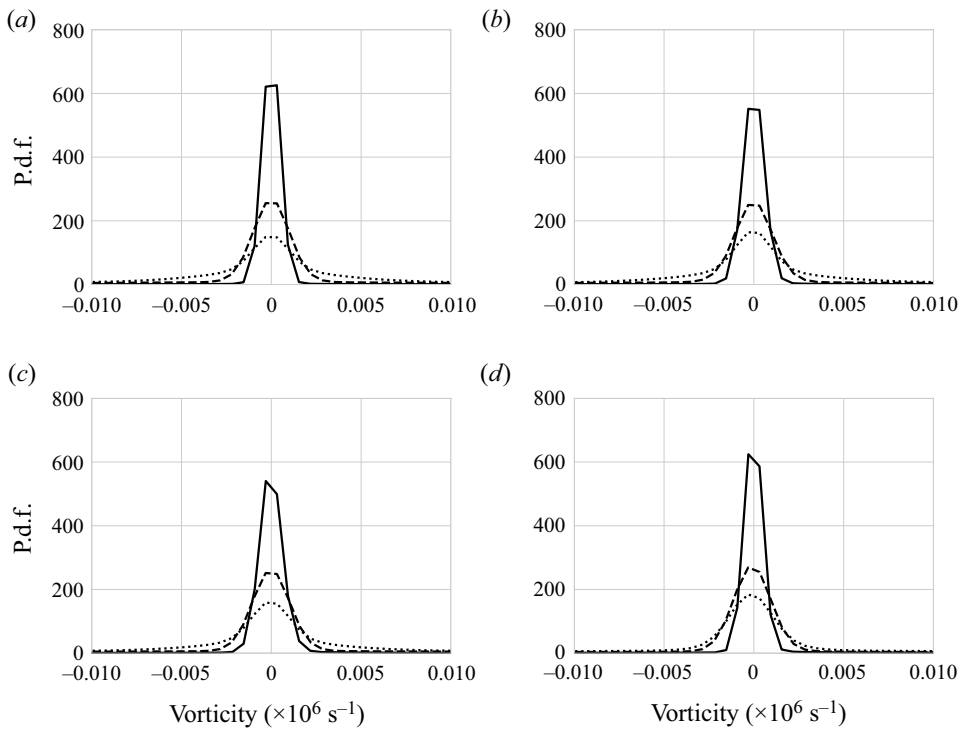
Figure 19. P.d.f.s of vorticity ω_z for columns with different initial tilt angles α_0, at different times τ: 5.7 (solid line), 35.7 (dashed line), and 110.8 (dotted line). Angles are (a) 1°, (b) 5°, (c) 10° and (d) 30°.

column angles and approaches nearly the same value ($\approx$0.063) for each column angle. That is, at later times, most gas exists in a lower concentration independent of the initial gas column angle. Similar tendencies are observed for the standard deviation.

More variation is observed with time and at different column angles in the skewness and kurtosis values (table 4). As time progresses, the skewness tends towards negative values, and more so as the column angle increases. Somewhat similar dynamics are observed for the kurtosis.
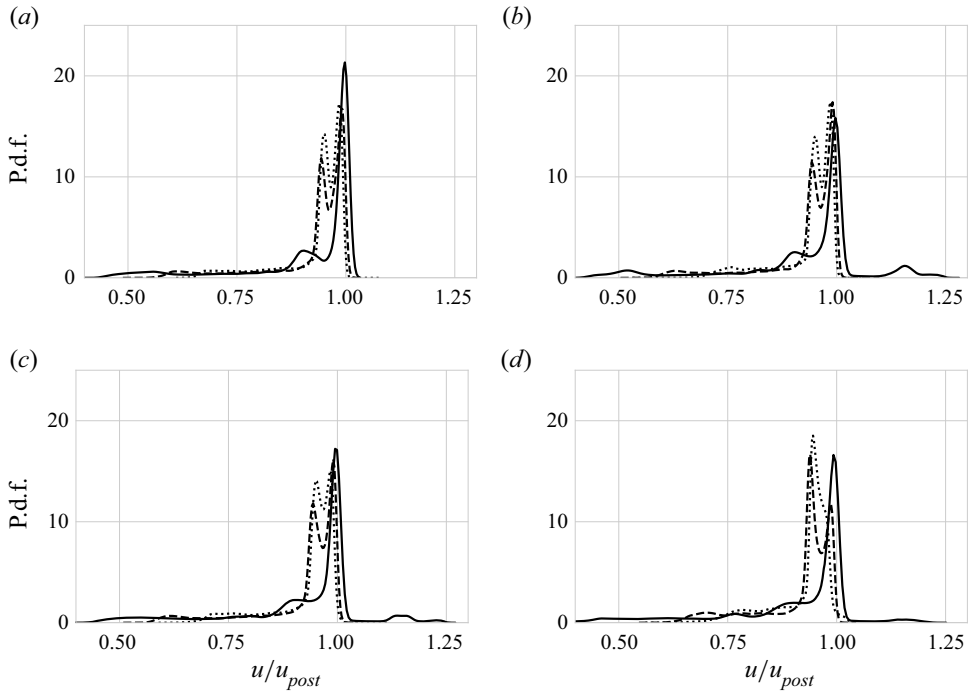
Figure 20. P.d.f.s of the *x*-component of velocity normalized by the post-shock velocity u_{post} at different times τ: 5.7 (solid line), 35.7 (dashed line), and 110.8 (dotted line). Angles are (*a*) $1°$, (*b*) $5°$, (*c*) $10°$ and (*d*) $30°$.

Figure 19 shows p.d.f.s of the *z*-component of vorticity that were constructed in the same way as the p.d.f.s of mass fraction. As the figure demonstrates, the column angle has little effect on the p.d.f. of this parameter and how its shape changes with time. At any time, the mean vorticity value is located around zero, with the p.d.f. shape being symmetric. With time, the distribution widens. However, at the largest column angle, $30°$, the range of vorticity values does not change much between $\tau \approx 35.7$ and $\tau \approx 110.8$, which explains the larger mean value at $\tau \approx 110.8$ to compare with those at the other angles at the same time.

Plots of p.d.f.s of the *x*-component of the gas velocity are presented in figure 20. At all considered gas column angles, a bimodal distribution emerges over time with two peaks: an upper peak corresponding to $u/u_{post} = 1$, and a lower peak between 0.90 and 0.95. The positions of the peaks are not influenced significantly by the column angle, and have similar behaviour over time for each initial column angle. However, their amplitudes vary with time and depend on the column angle. In particular, smaller column angles have a higher initial concentration of velocity around the lower peak, but over time, the higher column angles have a larger concentration of velocity around the lower peak. The opposite is observed for the upper peak.

P.d.f.s of the *y*-component of the gas velocity are shown in figure 21. At the smallest column angle, there is a single peak value for *y*-velocity around $v/u_{post} = 0$. With time, the distribution widens slightly, with gas starting to move in the vertical direction.

As the column angle increases, the initial distribution widens. Over time, larger initial column angles develop a bimodal distribution of velocity in the *y*-direction, with a positive and negative mean. At $\alpha \geqslant 10°$, the second peak becomes obvious with time. Both peaks have similar values at $\tau = 21.4$, and their locations are shifted from 0 m s^{-1} to
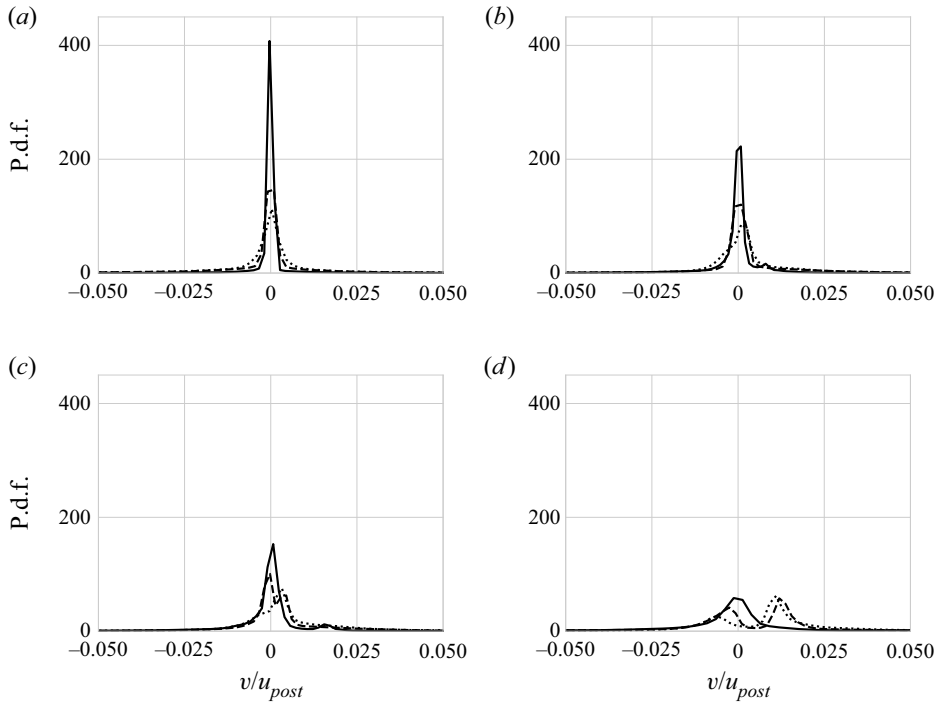
971 A26-24

Figure 21. P.d.f.s of the y-component of velocity normalized by the post shock velocity u_{post} at different times τ: 5.7 (solid line), 35.7 (dashed line), and 110.8 (dotted line). Angles are (*a*) $1°$, (*b*) $5°$, (*c*) $10°$ and (*d*) $30°$.

negative and positive values. At the latest time, $\tau = 110.8$, only one peak remains in the p.d.f., corresponding to $\alpha = 10°$, with the peak value being positive ($v/u_{post} \approx 0.003$). This again indicates gas moving upwards. At the largest column angle, $\alpha = 30°$, both peaks are seen at $\tau = 110.8$ (figure 21*d*), but the peak with the positive value is larger ($v/u_{post} \approx 0.013$), showing that more gas is moving upwards than downwards.

The component of gas velocity in the z-direction (shown in figure 22) maintains a narrow distribution around $w/u_{post} = 0$ for all initial column angles. Over time, the distribution widens slightly for smaller initial column angles. The zero mean is due to the symmetry of the sample plane, as discussed previously.

It is informative to compare the p.d.f.s of the SF_6 mass fraction (figure 18) with the experimental p.d.f.s of PLIF intensity in a very similar flow (figure 16 of Olmstead *et al.* 2017*a*). While the relationships of the overall trends for the mixing-driven p.d.f. time evolution in the flow are clear, the PLIF intensity p.d.f.s are dominated by a peak corresponding to the tracer-free (no fluorescence) flow, which is understandably absent from figure 18.

4. Conclusion

High-resolution viscous simulations were conducted to model the 3-D interaction between a planar shock and an inclined cylindrical column of heavy gas with an initially diffuse density interface. The overall flow morphology was similar to the inviscid case presented in our previous study (Romero *et al.* 2022). However, the increased resolution allowed for more detailed statistics to be collected. The effects of initial column angle on statistical properties of the flow were analysed.
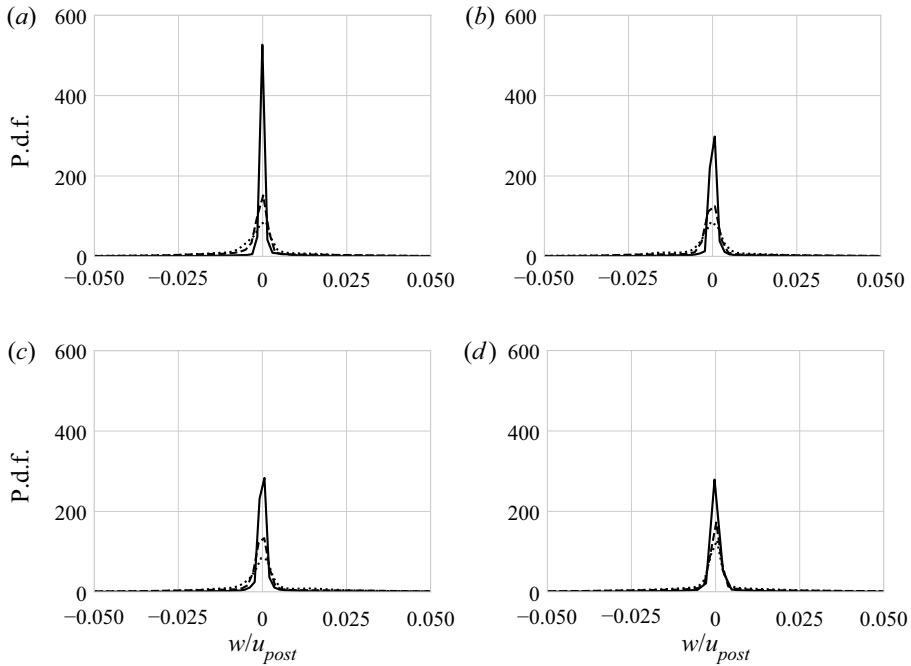
971 A26-25

Figure 22. P.d.f.s of the *z*-component of velocity normalized by the post shock velocity u_{post} at different times τ: 5.7 (solid line), 35.7 (dashed line), and 110.8 (dotted line). Angles are (*a*) $1°$, (*b*) $5°$, (*c*) $10°$ and (*d*) $30°$.

In particular, the analysis of mean velocity profiles showed that the streamwise velocity component is at the maximum near the column edges at all times. The magnitude of the vertical component initially has a maximum in the interior of the column, but approaches zero everywhere over time. The spanwise component is close to zero at all times everywhere due to the symmetry of the cross-sectional plane.

The intensities of all fluctuating velocities and of the shear stresses initially have a maximum near the centre (interior) of the column. Over time, the peak values of all Reynolds stresses move towards the leading edge of the column. The trailing edge of the column does not experience significant velocity fluctuations at any time.

Analysis of the anisotropy tensor shows that turbulent kinetic energy is non-uniformly distributed through the column. At larger column angles, turbulence tends towards isotropy in the column interior in the *y*- and *z*-components mainly. Anisotropy-invariant maps show that the turbulent state is near to that of single-component turbulence at early times, and that the flow moves in the direction of isotropy over time.

Analysis of the mixedness over time showed that the initial angle has very little effect on the mixing rate.

A power-law scaling with the exponent close to -1 was observed in the turbulent kinetic energy spectra at large wavenumbers. This scaling is similar to the power-law scaling for scalar structure functions obtained in some experiments. However, the scalar structure functions for the mass fraction based on the simulation data do not follow the power law except for large initial column angles at early times. The scalar field (mass fraction) structure function behaviour in our simulation is overall quite similar to that observed in experiment (tracer fluorescence intensity fields).

The mean and the standard deviation of the mass fraction p.d.f.s were found to be independent of the column angle, while both the skewness and the kurtosis generally
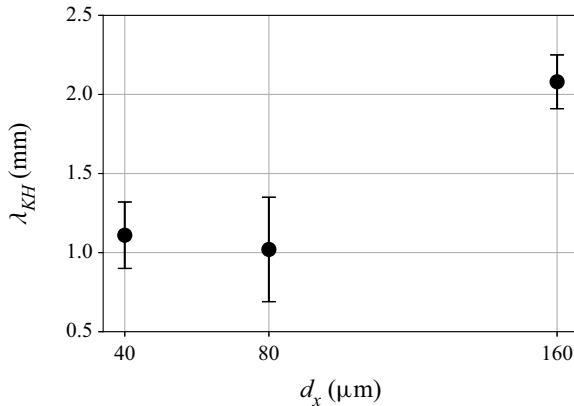
971 A26-26

Figure 23. KH wavelengths λ_{KH} at different grid sizes for a column with initial tilt angle $30°$. Error bars indicate one standard deviation.

decrease as the initial column angle increases. Vorticity is distributed symmetrically around 0 and does not have a significant dependence on initial column angle. Both x- and y-components of velocity tend towards a bimodal distribution as the initial column tilt angle is increased. The z-component of velocity maintains a narrow distribution around zero, as expected due to the symmetry of the sample plane.

Declaration of interests. The authors report no conflict of interest.

Author ORCIDs.
- Brian E. Romero https://orcid.org/0000-0001-8731-8836;
- Peter Vorobieff https://orcid.org/0000-0003-0631-7263;
- Svetlana V. Poroseva https://orcid.org/0000-0002-8102-4359.

Appendix A. Grid convergence

Here, grid sensitivity analysis results are presented for simulations of the gas column initially inclined at $30°$ and with Mach number 2.0. The grid resolutions considered are $dx = 40$ μm, 80 μm and 160 μm – that is, two additional grid resolutions, which are coarser than the grid used for the results presented in the main text. Simulations on finer grids could not be conducted due to insufficient computational resources.

The behaviour of the KH wavelengths with respect to grid cell size is shown in figure 23. As described previously, the KH wavelength λ_{KH} was determined by visually identifying wave peaks when they first become visible after shock passage, and measuring the distance between them. For each case, at least ten consecutive wave peaks were identified. The figure shows the average wavelength, along with error bars indicating one standard deviation. As the plot shows, the two finest grids considered, 40 μm and 80 μm, agree
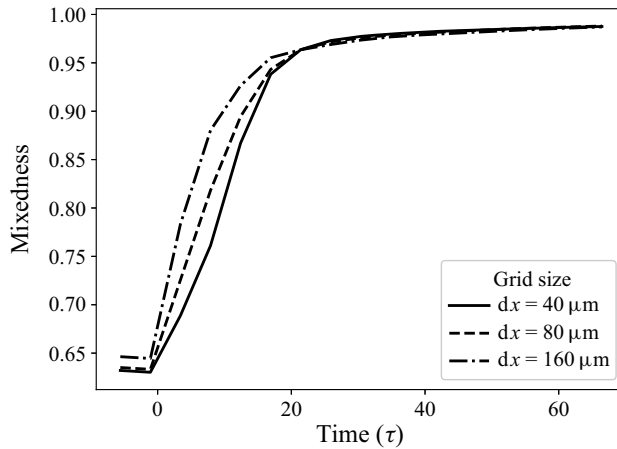
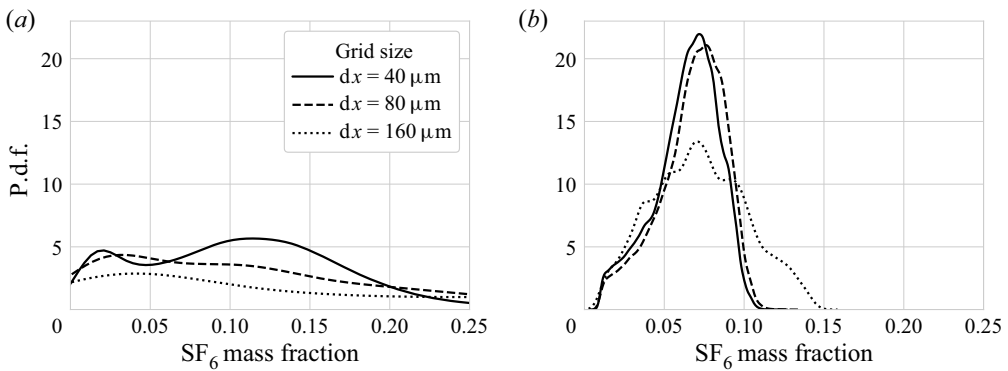Figure 24. Molecular mixedness over time for different grid resolutions.

Figure 25. P.d.f.s of SF_6 mass fraction Y_s for different grid resolutions at (*a*) $\tau = 5.7$ and (*b*) $\tau = 110.8$.

with regard to λ_{KH}, while the 160 μm grid overpredicts wavelengths by a factor of about two.

Effects of the grid cell size on the molecular mixedness were also considered and are presented in figure 24. As the figure demonstrates, the coarser grids predict a higher mixing rate than the finest grid at early times. This may be due to the averaging effect of the larger grid cells, which are unable to resolve fine-scale concentration fluctuations. At later times, however, the grid size has no distinguishable effect on the mixing efficiency.

P.d.f.s of SF_6 mass fraction are shown in figure 25 for the grids at two different times. At early times ($\tau = 5.7$), there is a higher probability of SF_6 mass fraction in the range from 0.05 to 0.2 for the $dx = 40$ μm grid when compared to the coarser grids. This peak at higher mass fractions results in the lower mixedness of the fine grid at early times, as seen in figure 24. At $\tau = 35.7$ (figure 25*b*), SF_6 distributions for $dx = 40$ μm and 80 μm are very similar, while the mass fraction distribution for the coarsest grid, though it has the same mean, is much wider. Nonetheless, the coarse grid shows identical mixedness to the finer grids despite the larger variance. The SF_6 mass fraction distribution converges faster with respect to grid size at late times than it does at early times, where it is more sensitive to grid size.

A similar phenomenon is observed for energy spectra. At early times, in this case $\tau = 35.7$ (figure 26*a*) after the flow has become turbulent, the coarse grids underestimate the spectral energy when compared to the finest grid. At later times ($\tau = 65.7$, figure 26*b*),
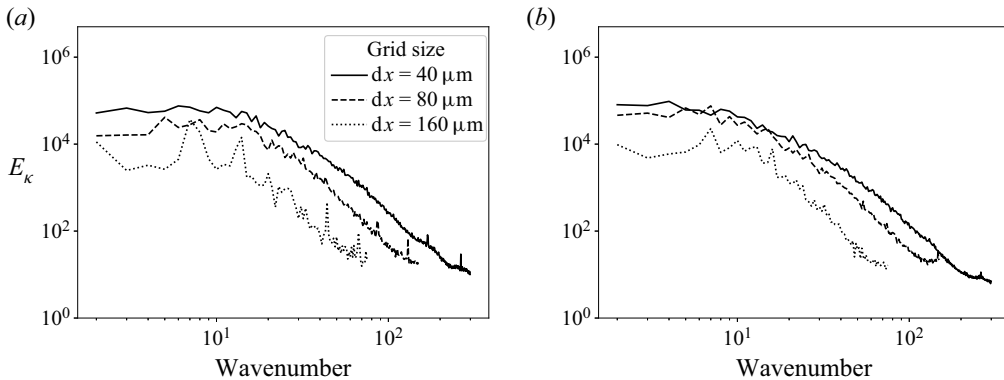
971 A26-28

Figure 26. Mean turbulent kinetic energy spectra in the vertical plane for different grid resolutions at (*a*) $\tau = 35.7$ and (*b*) $\tau = 65.7$.

the spectra for the two finest grids are in better agreement, while the coarse grid severely underpredicts spectral energy by an order of magnitude.

In general, the flow geometry, in terms of λ_{KH}, is well represented by the $dx = 40\ \mu m$ grid, and late-time mixedness and mass fraction p.d.f.s are converged. Early-time statistics, however, are more sensitive to grid resolution.

REFERENCES

ABARZHI, S.I. & SREENIVASAN, K.R. 2022 Self-similar Rayleigh–Taylor mixing with accelerations varying in time and space. *Proc. Natl Acad. Sci. USA* **119** (47), e2118589119.

ASAY-DAVIS, X.S., MARCUS, P.S., WONG, M.H. & DE PATER, I. 2009 Jupiter's shrinking Great Red Spot and steady Oval BA: velocity measurements with the 'Advection Corrected Correlation Image Velocimetry' automated cloud-tracking method. *Icarus* **203** (1), 164–188.

BOCCHIO, M., JONES, A.P. & SLAVIN, J.D. 2014 A re-evaluation of dust processing in supernova shock waves. *Astron. Astrophys.* **570**, A32.

BROUILLETTE, M. 2002 The Richtmyer–Meshkov instability. *Annu. Rev. Fluid Mech.* **34** (1), 445–468.

CELANI, A., CENCINI, M., VERGASSOLA, M., VILLERMAUX, E. & VINCENZI, D. 2005 Shear effects on passive scalar spectra. *J. Fluid Mech.* **523**, 99–108.

CHEVALIER, R.A., BLONDIN, J.M. & EMMERING, R.T. 1992 Hydrodynamic instabilities in supernova remnants – self-similar driven waves. *Astrophys. J.* **392**, 118–130.

DALTON, J. 1802 Essay IV. On the expansion of elastic fluids by heat. *Manchester Lit. Phil. Soc. Mem. Proc.* **5**, 595–602.

EDWARDS, H.C., TROTT, C.R. & SUNDERLAND, D. 2014 Kokkos: enabling manycore performance portability through polymorphic memory access patterns. *J. Parallel Distrib. Comput.* **74** (12), 3202–3216.

FAVRE, A., KOVASZNAY, L.S.G., DUMAS, R., GAVIGLIO, J. & COANTIC, M. 1976 *La turbulence en mécanique des fluides: bases théoriques et expérimentales, méthodes statistiques*. Gauthier-Villars.

GEORGE, W.K. 1992 The decay of homogeneous isotropic turbulence. *Phys. Fluids* A **4** (7), 1492–1509.

GOTO, S. & VASSILICOS, J.C. 2016 Unsteady turbulence cascades. *Phys. Rev.* E **94** (5), 053108.

GOWARDHAN, A.A. & GRINSTEIN, F.F. 2011 Numerical simulation of Richtmyer–Meshkov instabilities in shocked gas curtains. *J. Turbul.* **12**, N43.

GROOM, M. & THORNBER, B. 2019 Direct numerical simulation of the multimode narrowband Richtmyer–Meshkov instability. *Comput. Fluids* **194**, 104309.

HAHN, M., DRIKAKIS, D., YOUNGS, D.L. & WILLIAMS, R.J.R. 2011 Richtmyer–Meshkov turbulent mixing arising from an inclined material interface with realistic surface perturbations and reshocked flow. *Phys. Fluids* **23** (4), 046101.

HOLDER, D.A. & BARTON, C.J. 2004 Shock tube Richtmyer–Meshkov experiments: inverse chevron and half height. In *Proceedings of the Ninth International Workshop on the Physics of Compressible Turbulent Mixing*. IWPCTM.

HUANG, Y., TANG, H., LI, J. & ZHANG, C. 2012 Studies of DDT enhancement approaches for kerosene-fueled small-scale pulse detonation engines applications. *Shock Waves* **22** (6), 615–625.

JIANG, G.-S. & SHU, C.-W. 1996 Efficient implementation of weighted ENO schemes. *J. Comput. Phys.* **126** (1), 202–228.

KANE, J., DRAKE, R.P. & REMINGTON, B.A. 1999 An evaluation of the Richtmyer–Meshkov instability in supernova remnant formation. *Astrophys. J.* **511** (1), 335.

KUMAR, S., MENEVEAU, C. & EYINK, G. 2022 Perturbative model for the second-order velocity structure function tensor in turbulent shear flows. *Phys. Rev. Fluids* **7** (6), 064601.

KUMAR, S., ORLICZ, G., TOMKINS, C., GOODENOUGH, C., PRESTRIDGE, K., VOROBIEFF, P. & BENJAMIN, R. 2005 Stretching of material lines in shock-accelerated gaseous flows. *Phys. Fluids* **17** (8), 082107.

LINDL, J.D., MCCRORY, R.L. & CAMPBELL, E.M. 1992 Progress toward ignition and burn propagation in inertial confinement fusion. *Phys. Today* **45** (9), 32–40.

MARTINS, F.J.W.A., KIRCHMANN, J., KRONENBURG, A. & BEYRAU, F. 2021 Quantification and mitigation of PIV bias errors caused by intermittent particle seeding and particle lag by means of large eddy simulations. *Meas. Sci. Technol.* **32** (10), 104006.

MELTON, L.A. & LIPP, C.W. 2003 Criteria for quantitative PLIF experiments using high-power lasers. *Exp. Fluids* **35** (4), 310–316.

MENDIS, D.A. & ROSENBERG, M. 1994 Cosmic dusty plasma. *Annu. Rev. Astron. Astrophys.* **32** (1), 419–463.

MESHKOV, E.E. 1969 Instability of the interface of two gases accelerated by a shock wave. *Sov. Fluid Dyn.* **4** (5), 101–104.

MONIN, A.S. & YAGLOM, A.M. 2013 *Statistical Fluid Mechanics, Volume II: Mechanics of Turbulence*. Courier Corporation.

OLMSTEAD, D., WAYNE, P., SIMONS, D., MONJE, I.T., YOO, J.H., KUMAR, S., TRUMAN, C.R. & VOROBIEFF, P. 2017*a* Shock-driven transition to turbulence: emergence of power-law scaling. *Phys. Rev. Fluids* **2** (5), 052601.

OLMSTEAD, D., WAYNE, P., YOO, J.-H., KUMAR, S., TRUMAN, C.R. & VOROBIEFF, P. 2017*b* Experimental study of shock-accelerated inclined heavy gas cylinder. *Exp. Fluids* **58** (6), 71.

PALEKAR, A., VOROBIEFF, P. & TRUMAN, C.R. 2007 Two-dimensional simulation of a shock-accelerated gas cylinder. *Prog. Comput. Fluid Dyn.* **7** (8), 427.

PALMER, J. & HANSON, R. 1994 PLIF measurements of temperature and velocity in a reacting supersonic free jet with OH. *AIAA Paper* 1994-618.

PANDAS DEVELOPMENT TEAM 2020 Pandas-dev/pandas: Pandas. doi:10.5281/zenodo.3509134.

POPE, S.B. 2000 *Turbulent Flows*. Cambridge University Press.

PRESTRIDGE, K., RIGHTLEY, P.M., VOROBIEFF, P., BENJAMIN, R.F. & KURNIT, N.A. 2000 Simultaneous density-field visualization and PIV of a shock-accelerated gas curtain. *Exp. Fluids* **29** (4), 339–346.

RAMANI, R., REISNER, J. & SHKOLLER, S. 2019*a* A space–time smooth artificial viscosity method with wavelet noise indicator and shock collision scheme, Part 1: the 1-D case. *J. Comput. Phys.* **387**, 81–116.

RAMANI, R., REISNER, J. & SHKOLLER, S. 2019*b* A space–time smooth artificial viscosity method with wavelet noise indicator and shock collision scheme, Part 2: the 2-D case. *J. Comput. Phys.* **387**, 45–80.

RASMUS, A.M., *et al.* 2019 Shock-driven hydrodynamic instability of a sinusoidally perturbed, high-Atwood number, oblique interface. *Phys. Plasmas* **26**, 62103.

RICHTMYER, R.D. 1960 Taylor instability in shock acceleration of compressible fluids. *Commun. Pure Appl. Maths* **13** (2), 297–319.

ROMERO, B. 2021 Fiesta: fast, interface evolution, shocks, and transition in the atmosphere. University of New Mexico.

ROMERO, B., POROSEVA, S., VOROBIEFF, P. & REISNER, J. 2021*a* Simulations of the shock-driven Kelvin–Helmholtz instability in inclined gas curtains. *Phys. Fluids* **33**, 064103.

ROMERO, B., VOROBIEFF, P., POROSEVA, S.V. & REISNER, J.M. 2021*b* Three-dimensional validation exercise for Fiesta code: evolution of shock-driven instabilities. *WIT Trans. Engng Sci.* **132**, 3–11.

ROMERO, B.E., POROSEVA, S., VOROBIEFF, P. & REISNER, J. 2021*c* Shock driven Kelvin–Helmholtz instability. *AIAA Paper* 2021-0051.

ROMERO, B.E., POROSEVA, S., VOROBIEFF, P. & REISNER, J. 2022 Three-dimensional simulations of a shock–gas column interaction. *AIAA Paper* 2022-1072.

SMITH, A.V., HOLDER, D.A., BARTON, C.J., MORRIS, A.P. & YOUNGS, D.L. 2001 Shock tube experiments on Richtmyer–Meshkov instability across a Chevron profiled interface. In *Proceedings of the Eighth International Workshop on the Physics of Compressible Turbulent Mixing*. IWPCTM.

SREENIVASAN, K.R. 1996 The passive scalar spectrum and the Obukhov–Corrsin constant. *Phys. Fluids* **8** (1), 189–196.

SREENIVASAN, K.R. 2019 Turbulent mixing: a perspective. *Proc. Natl Acad. Sci. USA* **116** (37), 18175–18183.

THORNBER, B., GROOM, M. & YOUNGS, D. 2018 A five-equation model for the simulation of miscible and viscous compressible fluids. *J. Comput. Phys.* **372**, 256–280.

TOKUMARU, P.T. & DIMOTAKIS, P.E. 1995 Image correlation velocimetry. *Exp. Fluids* **19** (1), 1–15.

TOMKINS, C., PRESTRIDGE, K., RIGHTLEY, P., MARR-LYON, M., VOROBIEFF, P. & BENJAMIN, R. 2003 A quantitative study of the interaction of two Richtmyer–Meshkov-unstable gas cylinders. *Phys. Fluids* **15** (4), 986–1004.

TRITSCHLER, V.K., OLSON, B.J., LELE, S.K., HICKEL, S., HU, X.Y. & ADAMS, N.A. 2014 On the Richtmyer–Meshkov instability evolving from a deterministic multimode planar interface. *J. Fluid Mech.* **755**, 429–462.

VILLERMAUX, E., INNOCENTI, C. & DUPLAT, J. 2001 Short circuits in the Corrsin–Obukhov cascade. *Phys. Fluids* **13** (1), 284–289.

VOROBIEFF, P., ANDERSON, M., CONROY, J., WHITE, R., TRUMAN, C.R. & KUMAR, S. 2011 Vortex formation in a shock-accelerated gas induced by particle seeding. *Phys. Rev. Lett.* **106** (18), 184503.

VOROBIEFF, P., MOHAMED, N.-G., TOMKINS, C., GOODENOUGH, C., MARR-LYON, M. & BENJAMIN, R.F. 2003 Scaling evolution in shock-induced transition to turbulence. *Phys. Rev.* E **68** (6), 065301.

VOROBIEFF, P., TOMKINS, C., KUMAR, S., GOODENOUGH, C., MOHAMED, N.G. & BENJAMIN, R.F. 2004 Secondary instabilities in shock-induced transition to turbulence. *WIT Trans. Engng Sci.* **45**, 139–148.

WAYNE, P., OLMSTEAD, D., VOROBIEFF, P., TRUMAN, C.R. & KUMAR, S. 2015 Oblique shock interaction with a cylindrical density interface. *WIT Trans. Engng Sci.* **89**, 161–169.

WILLIAMSON, J.H. 1980 Low-storage Runge–Kutta schemes. *J. Comput. Phys.* **35** (1), 48–56.

WOITKE, P. 2006 2D models for dust-driven AGB star winds. *Astron. Astrophys.* **452** (2), 537–549.

WONG, M.L., LIVESCU, D. & LELE, S.K. 2019 High-resolution Navier–Stokes simulations of Richtmyer–Meshkov instability with reshock. *Phys. Rev. Fluids* **4** (10), 104609.

YANG, J., KUBOTA, T. & ZUKOSKI, E.E. 1993 Applications of shock-induced mixing to supersonic combustion. *AIAA J.* **31** (5), 854–862.

ZHAI, Z., DONG, P., SI, T. & LUOA, X. 2016 The Richtmyer–Meshkov instability of a 'V' shaped air/helium interface subjected to a weak shock. *Phys. Fluids* **28**, 82104.

ZHOU, Y. 2017a Rayleigh–Taylor and Richtmyer–Meshkov instability induced flow, turbulence, and mixing. I. *Phys. Rep.* **720–722**, 1–136.

ZHOU, Y. 2017b Rayleigh–Taylor and Richtmyer–Meshkov instability induced flow, turbulence, and mixing. II. *Phys. Rep.* **723–725**, 1–160.